

## Study of halogen–carbon dioxide clusters and the fluoroformyloxyl radical by photodetachment of $X-(CO_2)$ ( $X=I, Cl, Br$ ) and $FCO-2$

Don W. Arnold, Stephen E. Bradforth, Eun H. Kim, and Daniel M. Neumark

Citation: *The Journal of Chemical Physics* **102**, 3493 (1995); doi: 10.1063/1.468575

View online: <http://dx.doi.org/10.1063/1.468575>

View Table of Contents: <http://scitation.aip.org/content/aip/journal/jcp/102/9?ver=pdfcov>

Published by the [AIP Publishing](#)

### Articles you may be interested in

Method of increments for the halogen molecular crystals: Cl, Br, and I  
J. Chem. Phys. **141**, 124707 (2014); 10.1063/1.4896230

A theoretical study of the  $CX_2N$  radicals ( $X = F, Cl, Br$ ): The effect of halogen substitution on structure, isomerization, and energetics  
J. Chem. Phys. **136**, 044316 (2012); 10.1063/1.3678006

$S \cdots X$  halogen bonds and  $H \cdots X$  hydrogen bonds in  $H_2CS-XY$  ( $XY = FF, ClF, ClCl, BrF, BrCl, \text{ and } BrBr$ ) complexes: Cooperativity and solvent effect  
J. Chem. Phys. **136**, 014302 (2012); 10.1063/1.3673540

Visible absorption spectroscopy of the  $B^2A_1-X^2B_2$  transition of fluoroformyloxyl radical,  $FC(O)O$   
J. Chem. Phys. **98**, 784 (1993); 10.1063/1.464241

Metal cluster oxidation: Chemiluminescence from the reaction of sodium polymers ( $Na_n, n \geq 3$ ) with halogen atoms ( $X = Cl, Br, I$ )  
J. Chem. Phys. **76**, 6439 (1982); 10.1063/1.443001



# Study of halogen-carbon dioxide clusters and the fluoroformyloxyl radical by photodetachment of $X^-(\text{CO}_2)$ ( $X=\text{I}, \text{Cl}, \text{Br}$ ) and $\text{FCO}_2^-$

Don W. Arnold,<sup>a)</sup> Stephen E. Bradforth,<sup>b)</sup> Eun H. Kim, and Daniel M. Neumark<sup>c)</sup>

Department of Chemistry, University of California, Berkeley, California, 94720

and Chemical Sciences Division, Lawrence Berkeley Laboratory, Berkeley, California 94720

(Received 12 September 1994; accepted 23 November 1994)

Photoelectron spectra have been measured for the anions  $X^-(\text{CO}_2)$ , with  $X=\text{I}, \text{Br}, \text{Cl}$ , and  $\text{F}$ . The vibrationally resolved spectra show that  $\text{I}^-(\text{CO}_2)$ ,  $\text{Br}^-(\text{CO}_2)$ , and  $\text{Cl}^-(\text{CO}_2)$  are primarily electrostatically bound clusters, although the charge-quadrupole interaction is strong enough to distort the  $\text{CO}_2$  molecule by as much as  $10^\circ$  [in  $\text{Cl}^-(\text{CO}_2)$ ]. *Ab initio* calculations and electrostatic models are used to describe the geometry and bonding of these clusters. The photoelectron spectrum of  $\text{FCO}_2^-$  is qualitatively different and shows transitions to both the  $\tilde{X}^2B_2$  ground and the  $\tilde{A}^2A_2$  first excited electronic states of the covalently bound  $\text{FCO}_2$  radical. The previously unobserved  $\tilde{A}^2A_2$  state is measured to lie 0.579 eV above the ground state. Vibrational frequencies are assigned with the assistance of *ab initio* calculations. The  $\text{FCO}_2$  heat of formation is determined to be  $\Delta_f H_{298}^0(\text{FCO}_2) = -85.2 \pm 2.8$  kcal/mol. While both  $\text{FCO}_2^-$  and  $\text{FCO}_2$  are more strongly bound than the other halide- $\text{CO}_2$  clusters, the C-F bonds are very weak relative to C-F bonds found in other halocarbon compounds. © 1995 American Institute of Physics.

## I. INTRODUCTION

The central role that solvation plays in the chemical sciences is well recognized. As a result, the fundamental basis of solvation remains an active topic of chemical physics. The major goal of these studies is to generate a model which can explain and predict solvation dynamics based upon the chemical properties of each component of a solute/solvent pair. In order to understand solvation on a microscopic level, it is important to first understand the interaction of binary solute/solvent complexes. One can then study the additional interactions which result as more solvent molecules are added, until the bulk solvation limit is reached. Spectroscopic studies of size-selected cluster ions represent an attractive experimental approach to this problem. In this paper, the first of a two part series, we present photoelectron spectra of  $X^-(\text{CO}_2)$  complexes ( $X=\text{I}, \text{Br}, \text{Cl}, \text{F}$ ) which demonstrate how the  $X\text{--CO}_2$  bonding character changes from a very weak interaction to a covalent bond, in both the anion and the neutral, as  $X$  varies from  $\text{I}$  to  $\text{F}$ . The second paper, which follows, describes how the cluster properties change as additional  $\text{CO}_2$  molecules are added to the anion.

The nature of the interaction between halide anions and  $\text{CO}_2$  has been studied for several years. Spears and co-workers<sup>1</sup> studied  $\text{F}^-\text{--CO}_2$  both experimentally and theoretically. From their studies, they found that electrostatic calculations were insufficient to describe their measured C-F bond strength ( $\Delta H \sim 18$  kcal/mol).<sup>1(b)</sup> McMahon and co-workers<sup>2</sup> used ion cyclotron resonance (ICR) techniques to measure the gas phase Lewis acidities of many systems and bracketed the value of the  $\text{CO}_2$  fluoride affinity as  $D_0(\text{F}^-\text{--CO}_2) = 31.7 \pm 2$  kcal/mol. On the other hand,

$D_0(X^-\text{--CO}_2)$  is considerably smaller for  $X=\text{Cl}, \text{Br}$ , and  $\text{I}$ ; high pressure mass spectrometry data<sup>3,4</sup> indicate that the binding energies of the heavier halides are between 5–8 kcal/mol. This significant difference in bond energies implies that a qualitatively different type of bonding is present for  $\text{FCO}_2^-$ , relative to the other  $X^-(\text{CO}_2)$  complexes.

Two of the anions have been studied previously by spectroscopic methods. Ault<sup>5</sup> investigated the matrix isolated  $\text{FCO}_2^-$  anion complexed with a  $\text{Cs}^+$  counterion. Three vibrational frequencies were measured and assigned to the CF symmetric stretch ( $883\text{ cm}^{-1}$ ), the CO symmetric stretch ( $1316\text{ cm}^{-1}$ ), and the CO antisymmetric stretch ( $1749\text{ cm}^{-1}$ ). Photoelectron spectra have been previously reported for the  $\text{I}^-(\text{CO}_2)_n$  clusters.<sup>6,7</sup> In addition, the  $\text{I}^-(\text{CO}_2)$  cluster has been investigated at higher resolution with negative ion zero electron kinetic energy (ZEKE) spectroscopy.<sup>8</sup> *Ab initio* calculations on  $\text{FCO}_2^-$  and  $\text{Cl}^-(\text{CO}_2)$  have been carried out by Nguyen<sup>9</sup> and Hiraoka *et al.*,<sup>4</sup> respectively. These calculations predict that the interaction between the  $X^-$  and  $\text{CO}_2$  is sufficiently strong to distort the  $\text{CO}_2$  from linearity, with considerably more distortion in  $\text{FCO}_2^-$ .

Information on the neutral  $\text{XCO}_2$  species is limited to the above photodetachment studies of the  $\text{I}^-(\text{CO}_2)$  cluster, which probed the  $\text{I--CO}_2$  van der Waals complex, and a few studies of the  $\text{FCO}_2$  radical. The  $\text{FCO}_2$  radical has been proposed as a reactive intermediate the  $\text{O+FCO} \rightarrow \text{F+CO}_2$  reaction,<sup>10</sup> an important contributor to the F atom production in  $\text{O}_2/\text{CF}_4$  plasmas commonly used to etch the Si or  $\text{SiO}_2$  surfaces of microelectronics devices.<sup>11</sup> The  $\text{FCO}_2$  radical is also believed to be produced in the atmosphere by the oxidation of hydrofluorocarbons.<sup>12</sup> Maricq *et al.*<sup>13</sup> have recently observed a visible absorption band of the  $\text{FCO}_2$  radical which they assign as the  $B^2A_1 \leftarrow \tilde{X}^2B_2$  transition, and this has been used in subsequent studies to follow the kinetics of  $\text{FCO}_2$ .<sup>14,15</sup> Francisco *et al.*<sup>12</sup> have proposed that  $\text{FCO}_2$  is involved in catalytic  $\text{O}_3$  destruction cycles through its reactions with  $\text{O}_2$  and  $\text{NO}$ , although Wallington *et al.*<sup>15</sup> demonstrated

<sup>a)</sup>Current address: Department of Chemistry, University of Southern California, Los Angeles, CA 90025.

<sup>b)</sup>Current address: Department of Chemistry, University of Chicago, Chicago, IL 60637.

<sup>c)</sup>Camille and Henry Dreyfus Teacher-Scholar.

that these reactions are probably too slow to play a significant role in stratospheric chemistry. The thermodynamics of  $\text{FCO}_2$  were investigated in an *ab initio* study by Francisco<sup>10</sup> in which the F–C bond strength was found to be very weak, about 3.5 kcal/mol.

Our photoelectron spectra probe both the energetics and spectroscopy of the  $\text{X}^-(\text{CO}_2)$  and  $\text{X}\cdot\text{CO}_2$  series. For  $\text{X}=\text{Cl}$ ,  $\text{Br}$ , and  $\text{I}$ , the spectra show that the interactions in the anion and neutral binary complexes are relatively weak, and that the  $\text{X}$  and  $\text{CO}_2$  moieties are more or less intact. In the anions, the halide distorts the  $\text{CO}_2$  geometry from linearity, while in the neutral complexes, the  $\text{CO}_2$  perturbs the electronic structure of the open shell halogen atom. In contrast, the C–F interactions in  $\text{FCO}_2^-$  and  $\text{FCO}_2$ , are considerably stronger, suggesting that both species are better described as covalently bound molecules rather than weakly bound complexes. Our  $\text{FCO}_2^-$  photoelectron spectrum provides an experimental measure of the F–C bond strength in  $\text{FCO}_2$  as well as new spectroscopic information about its ground and first excited states.

The distortion of the  $\text{CO}_2$  in its complexes with the heavier halides is of considerable interest, since the mechanism causing this distortion is important in understanding the nature of the binding in these species. This distortion can arise from charge transfer from the halide to the  $\text{CO}_2$ , or from purely electrostatic interactions between the  $\text{X}^-$  and the nonspherical charge distribution of the  $\text{CO}_2$ . Although briefly addressed by other investigators,<sup>4</sup> we will consider in some detail the relative contributions of these two mechanisms. Our treatment is likely to be useful in considering distortion in other cluster ions such as  $\text{I}^-(\text{CH}_3\text{I})$ , for which Cyr *et al.* found that clustering to  $\text{I}^-$  leads to a significant elongation of the C–I bond in the  $\text{CH}_3\text{I}$  moiety.<sup>16</sup>

As a part of the data analysis, *ab initio* calculations for  $\text{FCO}_2^-$ ,  $\text{FCO}_2$ , and  $\text{Cl}^-(\text{CO}_2)$  have been performed. The  $\text{Cl}^-(\text{CO}_2)$  results are compared to the results of the electrostatic calculations used to investigate the nature of the X–C bonding. The  $\text{FCO}_2^-$  and  $\text{FCO}_2$  results are instrumental in the assignment of the observed spectral features for the ground and first excited electronic states of  $\text{FCO}_2$ .

## II. EXPERIMENT

The experiments are performed on a dual time-of-flight anion photoelectron spectrometer. A schematic diagram of the apparatus is shown in Fig. 1. Since a full description of the spectrometer has been given previously,<sup>17</sup> only a general overview with details relevant to these experiments will be given. By intersecting a pulsed molecular beam (1) with a 1 keV electron beam (2),<sup>18</sup> the anions of interest are formed as in Eq. (1),



The halide ions,  $\text{X}^-=\text{F}^-$ ,  $\text{Cl}^-$ ,  $\text{Br}^-$ , and  $\text{I}^-$ , are generated by dissociative attachment of low-energy ( $\sim 1$  eV) secondary electrons to  $\text{NF}_3$ ,  $\text{CF}_2\text{Cl}_2$ ,  $\text{HBr}$ , and  $\text{HI}$ , respectively. The molecular beam expansion typically consists of a 5% mix-

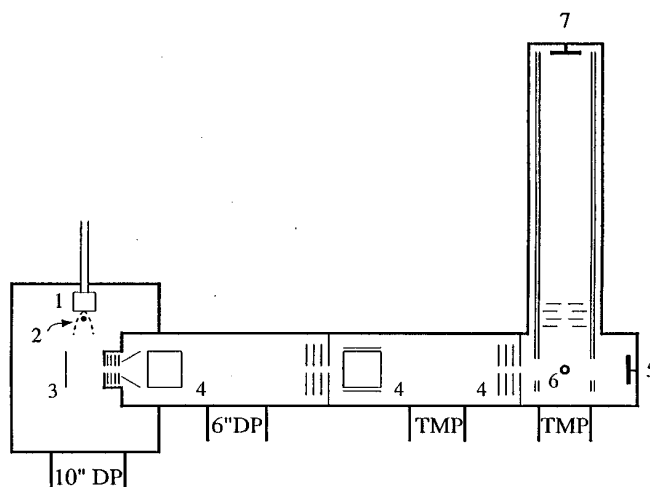


FIG. 1. Schematic diagram of the dual time-of-flight anion photoelectron spectrometer.

ture of the halogen source in  $\text{CO}_2$  at a backing pressure of  $\sim 4$  atm. As the expansion proceeds, the halide ions cluster or react with the carrier gas,  $M=\text{CO}_2$ , and the adduct relaxes rotationally and vibrationally by further collisions with the carrier gas during the remainder of the expansion.

The cooled ions are injected by a pulsed negative potential at (3) into a Wiley–McLaren-type time-of-flight mass spectrometer<sup>19</sup> where they separate according to mass. Ion levels are optimized with ion optics (4) to obtain maximum signal at the microchannel plate detector (5). The ion of interest is photodetached at (6) by a properly timed 8 ns laser pulse propagating perpendicular to the anion beam. Energies of the photoelectrons are determined by measurement of their time-of-flight through a 1 m field-free flight tube to a second microchannel plate detector (7). The resolution of the apparatus is 0.010 eV for electrons with 0.65 eV of electron kinetic energy (eKE) and degrades as  $\text{eKE}^{3/2}$ . In the  $\text{FCO}_2^-$  spectra, the resolution is slightly decreased by “space-charge” effects to 0.015 eV at 0.65 eV (see Sec. IV B 1). For these experiments, the 4th (266 nm; 4.657 eV; 15 mJ/pulse) and 5th harmonics (213 nm; 5.822 eV; 6 mJ/pulse) of a Nd:YAG pulsed laser (QuantaRay DCR3), are used for photodetachment. The plane polarized laser beam can be rotated with a half-wave plate in order to study photoelectron angular distributions.

Background electrons are generated by 213 nm photons which scatter and interact with the surfaces inside the detector region of the apparatus. Although laser and electron baffles are employed to discriminate against these background electrons, the 213 nm photons generate background levels which require a background subtraction procedure. A background spectrum, collected with the same laser power used during data collection, is fitted to a smooth function. This function is scaled and subtracted from the data to correct for the moderate level background signal.

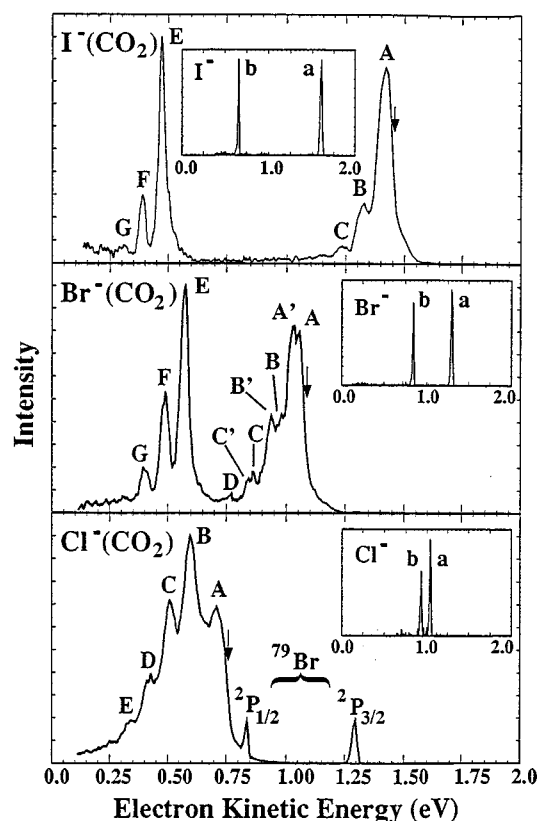


FIG. 2. Photoelectron spectra of  $\text{I}^-(\text{CO}_2)$ ,  $\text{Br}^-(\text{CO}_2)$ , and  $\text{Cl}^-(\text{CO}_2)$  using a 4.657 eV photodetachment energy. Spectra of  $\text{I}^-$ ,  $\text{Br}^-$ , and  $\text{Cl}^-$  are shown, for comparison, in the insets.

### III. RESULTS

#### A. Experiment

Shown in Fig. 2 are the photoelectron spectra obtained for  $\text{I}^-(\text{CO}_2)$ ,  $\text{Br}^-(\text{CO}_2)$ , and  $\text{Cl}^-(\text{CO}_2)$  at  $h\nu=4.657$  eV. Spectra of the bare halide atoms are shown in the corresponding insets. The spectra represent intensity of electron signal as a function of electron kinetic energy (eKE) where

$$\text{eKE} = h\nu - \text{EA} - T_0 - E_v^0 + E_v^- . \quad (2)$$

In Eq. (2),  $h\nu$  is the laser photon energy, EA is the electron affinity of the neutral species,  $T_0$  is the term value of the neutral electronic state.  $E_v^0$  and  $E_v^-$  are the vibrational energies (above the zero point energy) of the neutral and anion,

respectively. Rotational contributions to the molecular internal energy are neglected. Peak positions and widths for the three spectra are summarized in Table I.

In the insets in Fig. 2, the two peaks in each atomic halide spectrum represent photodetachment transitions from the closed-shell anion to the two spin-orbit states of the halogen atom; the  $^2P_{3/2}$  ground state and, at lower eKE, the  $^2P_{1/2}$  excited state. The EA and the spin-orbit splitting energies are well known for the halogens and are given in Table II.

As the halogen atom becomes lighter, the differences between the  $\text{X}^-(\text{CO}_2)$  and  $\text{X}^-$  spectra become more apparent. The  $\text{I}^-(\text{CO}_2)$  spectrum contains two bands whose apparent origins, peaks A and E, are separated by  $0.948 \pm 0.010$  eV, which is equal to the iodine spin-orbit splitting within experimental uncertainty. Thus, to first order, the bands at high and low eKE can be labeled as  $\text{I}(^2P_{3/2})\cdot\text{CO}_2$  and  $\text{I}(^2P_{1/2})\cdot\text{CO}_2$ , respectively. The band origins are shifted to lower eKE by 0.181 eV relative to peaks a and b in the  $\text{I}^-$  spectrum. Within each band, a progression extends to lower eKE. The average spacing for the progression beginning at 0.472 eV is  $\sim 665$   $\text{cm}^{-1}$ . All of the peaks in the spectrum are significantly broader than the experimental resolution as a result of unresolved underlying structure.<sup>8</sup> Additionally, the peaks at high eKE are significantly broader (68 meV FWHM) than those at low eKE (33 meV FWHM).

The  $\text{Br}^-(\text{CO}_2)$  spectrum also shows two distinct bands separated by  $0.460 \pm 0.008$  eV, essentially equal to the Br spin-orbit splitting. The bands are shifted by 0.233 eV towards lower eKE relative to the  $\text{Br}^-$  spectrum. However, in contrast to the  $\text{I}^-(\text{CO}_2)$  spectrum, the peaks in the  $\text{Br}(^2P_{3/2})\cdot\text{CO}_2$  progression at high eKE are split into doublet pairs. Deconvolution of the feature into two Gaussian shaped peaks reveals that the two peaks of each doublet are separated by about 280  $\text{cm}^{-1}$ . The raw spacing of the progression is  $\sim 750$   $\text{cm}^{-1}$ .

The  $\text{Cl}^-(\text{CO}_2)$  spectrum appears as one long progression of broad peaks. However, the A–B separation,  $\sim 900$   $\text{cm}^{-1}$ , is greater than the remaining peak spacings which are about 700  $\text{cm}^{-1}$ . The comparable energies of the vibrational spacings and the Cl spin-orbit splitting (880  $\text{cm}^{-1}$ ) suggests that the extra width of the peaks in the spectrum results from nearly overlapping transitions to the two spin-orbit bands of the neutral. Peak A is displaced by 0.355 eV with respect to the  $\text{Cl}(^2P_{3/2})\leftarrow\text{Cl}^-$  peak in the inset. As indicated in Fig. 3,

TABLE I. Peak positions and widths for  $\text{X}^-(\text{CO}_2)$  photoelectron spectra ( $\text{X}=\text{Cl}, \text{Br}, \text{I}$ ).

Peak	$\text{Cl}^-(\text{CO}_2)$		$\text{Br}^-(\text{CO}_2)$		$\text{I}^-(\text{CO}_2)$	
	eKE (eV)	FWHM	eKE (eV)	FWHM	eKE (eV)	FWHM
A	0.709	0.09	1.058	0.036	A'1.033	...
B	0.598	0.08	0.984	0.036	B'0.941	...
C	0.510	0.07	0.868	0.036	C'0.847	...
D	0.425	0.07	0.775	0.036	...	...
E	0.338	0.06	0.580	0.045	...	...
F	...	...	0.492	0.052	...	...
G	...	...	0.400	0.42	...	...

TABLE II. Halogen electron affinities and spin-orbit splittings.

Halogen	Electron affinity <sup>a</sup>	Spin-orbit splitting
F	3.401 190 eV	0.0510 eV <sup>b</sup>
Cl	3.612 69 eV	0.109 40 eV <sup>b</sup>
Br	3.365 90 eV	0.456 9 eV <sup>c</sup>
I	3.059 1 eV	0.942 68 eV <sup>c</sup>

<sup>a</sup>T. R. Miller in *CRC Handbook of Chemistry and Physics*, 72nd ed. edited by D. R. Lide (Chemical Rubber, Cleveland, 1991), pp. 10–180.

<sup>b</sup>S. Baskin and J. O. Stoner, Jr., *Atomic Energy Level and Grotian Diagrams* (North-Holland, New York, 1978), Vol. 2.

<sup>c</sup>C. E. Moore, *Atomic Energy Levels*, Vol. I, Natl. Stand. Ref. Data Ser. Natl. Bur. Stand. **35**, (1971).

the  $^{35}\text{Cl}^-(\text{CO}_2)$  spectrum contains contributions from  $^{79}\text{Br}^-$  detachment at higher eKE (0.834 and 1.300 eV) as a result of their identical masses. These “contaminant” peaks serve as a check of calibration accuracy.

Figure 3 shows the photoelectron spectra of  $\text{FCO}_2^-$  obtained at a photodetachment energy of 5.822 eV. The extensive vibrational structure covering an energy range of about 1.25 eV differs markedly from the other  $\text{X}^-(\text{CO}_2)$  spectra. A spectrum of  $\text{F}^-$ , also collected at this energy, is shown in the inset. The spin-orbit splitting of fluorine (0.0501 eV) is too small to be resolved at this high photodetachment energy because the electrons have  $>2.3$  eV of kinetic energy, where the spectral resolution is approximately 60 meV. The energy difference between peak A in the  $\text{FCO}_2^-$  spectrum and the  $\text{F}^-$

TABLE III. Peak positions for  $\text{FCO}_2^-$  photoelectron spectrum,  $h\nu=5.82$  eV.

Peak	eKE (eV)	Energy ( $\text{cm}^{-1}$ )
A	1.595	0
B	1.534	492
C	1.476	960
D	1.419	1420
E	1.360	1895
F	1.300	2379
G	1.246	2815
H	1.186	3299
I	1.129	3758
J	1.075	4194
K	1.016	4670
L	0.950	5202
M	0.904	5573
N	0.858	5944
O	0.785	6863
P	0.744	6863
Q	0.698	7234
R	0.628	7799
S	0.592	8090
T	0.540	8509

peak is 0.824 eV, considerably larger than shifts observed in the other  $\text{X}^-(\text{CO}_2)$  spectra. Overall, the observed features are better characterized as transitions between two molecular species than as photodetachment transitions of a solvated fluoride anion. The peak positions are summarized in Table III. A least-squares analysis of the peak spacings in progression A–J provides values of  $\omega_e=485\text{ cm}^{-1}$  and  $x_e\omega_e=2\text{ cm}^{-1}$ . Beginning at peak K, three progressions and their combination bands can be discerned in the irregularly spaced peaks. The average spacings of these three progressions are 540, 905, and  $1280\text{ cm}^{-1}$ .

As mentioned in Sec. II, the photoelectron angular distributions can be studied by varying the direction of the laser polarization. Equation (3) gives the expression for the differential photodetachment cross section,<sup>20</sup> where  $\sigma_{\text{tot}}(\text{eKE})$  is the total cross section for photodetachment,  $\beta(\text{eKE})$  is the asymmetry parameter ( $-1\leq\beta\leq 2$ ), and  $\theta$  is the angle between the electric vector of the laser beam and the direction of electron collection,

$$\frac{d\sigma}{d\Omega} = \frac{\sigma_{\text{tot}}(E)}{4\pi} \left[ 1 + \beta(E) \left( \frac{3}{2} \cos^2 \theta - \frac{1}{2} \right) \right]. \quad (3)$$

While  $\beta$  is not expected to change significantly over the energy range spanned by the vibrational progression, it can differ markedly for transitions to different electronic states. In such a case, Eq. (3) shows that the relative intensities of the corresponding electronic bands will vary with the laser polarization angle,  $\theta$ . Figure 3 shows the  $\text{FCO}_2^-$  spectrum collected at two different laser polarizations, as indicated. The intensity of progression A–J decreases by approximately 20% upon rotation from  $\theta=90^\circ$  to  $\theta=0^\circ$ , relative to peaks K–T. According to Eq. (3), this polarization dependence suggests that photodetachment transitions to two different electronic states are contributing to the spectrum; one state be-

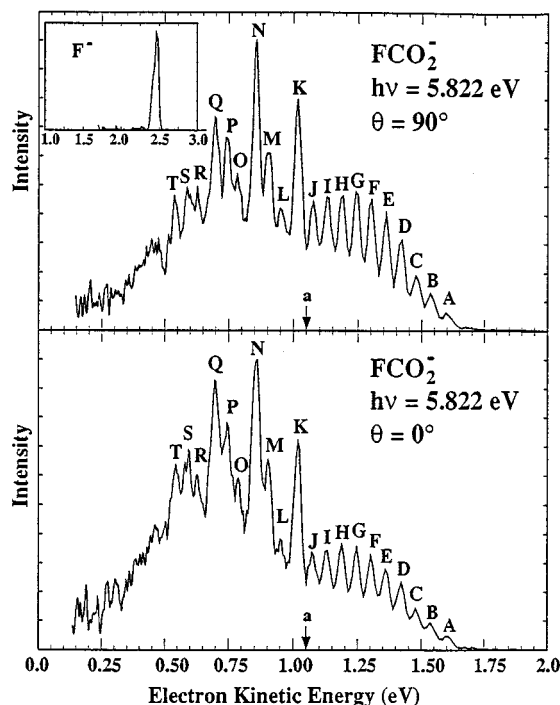


FIG. 3. Photoelectron spectra of  $\text{FCO}_2^-$  using a 5.822 eV photodetachment energy. The data are collected at two laser polarizations, as indicated. A spectrum of  $\text{F}^-$  is shown in the inset for comparison. The arrow labeled “a” indicates the  $\text{F}+\text{CO}_2$  dissociation asymptote for the fluoroformyloxyl radical.

TABLE IV. *Ab initio* calculations for  $\text{Cl}^-(\text{CO}_2)$ .

Level of theory	Energy (a.u.)	$R_{\text{Cl-Cl}}$ (Å)	$R_{\text{C-O}}$ (Å)	$\angle\text{OCO}$ (deg)
RHF/4-31G*	−646.520 925	2.879	1.146	168.2
RHF/6-31+G*	−647.186 564	3.241	1.145	173.2
RHF/6-311+G*	−647.265 090	3.256	1.137	173.6
MP2/31+G*	−647.799 755	2.974	1.183	170.9
MP2/6-311+G*	−647.920 816	2.992	1.172	171.6
MP4/6-31+G*	−647.839 376	2.943	1.190	169.9
MP4/6-311+G*	−647.962 047	2.972	1.180	170.9
Expt.	...	...	...	169.2±2.5

gins at peak A while the second begins at peak K. An analysis of the  $\text{FCO}_2^-$  spectrum, including peak assignments, is given in Sec. IV B 3.

As found previously for the isoelectronic  $\text{NO}_3^-$  anion,<sup>44</sup>  $\text{FCO}_2^-$  has an extremely low cross section for photodetachment. As a result, unusually high ion levels were required to obtain a satisfactory signal to noise ratio. At such high ion levels, the energy of the departing electron is significantly affected by Coulombic interactions with remaining undetached  $\text{FCO}_2^-$  ions in the laser interaction region. This interaction shifts the spectrum to higher eKE and broadens observed spectral features. The magnitude of the “space-charge” shift is determined by measurement of the shift for calibration ions (i.e.,  $\text{I}^-$ ,  $\text{Br}^-$ ,  $\text{Cl}^-$ , and  $\text{F}^-$ ) at the same ion densities used for the  $\text{FCO}_2^-$  data collection. For the  $\text{FCO}_2^-$  data, the shift is determined to be  $\sim 0.035$  eV, and the energy axis in Fig. 3 has been corrected appropriately. Through the same comparison, the broadening of the peaks is estimated to be  $\sim 0.005$  eV.

## B. *Ab initio* calculations

The following two sections describe *ab initio* calculations performed to aid in the interpretation of the data presented above. These calculations are aimed at determining the geometries of  $\text{Cl}^-(\text{CO}_2)$ ,  $\text{FCO}_2^-$ , and  $\text{FCO}_2$ . For  $\text{FCO}_2$ , several electronic states are investigated and the results are used in the assignment of the observed spectral features.

### 1. $\text{Cl}^-(\text{CO}_2)$

Previous calculations by Hiraoka *et al.*<sup>4</sup> at the SCF/4-31G+*p* level of show that the  $\text{CO}_2$  is slightly bent in  $\text{Cl}^-(\text{CO}_2)$ . We have extended these calculations to higher levels of theory which include electron correlation effects. Additionally larger basis sets are employed to better describe the diffuse negative charge on the complex.<sup>21</sup> At the SCF and Møller–Plesset (MP2 and MP4) levels of theory, calculations are carried out using 6-31+G\* and 6-311+G\* basis sets to determine the equilibrium geometry. The calculations were done using the GAUSSIAN92 *ab initio* package.<sup>22</sup> The results are summarized in Table IV. There is surprisingly good agreement between the HF/4-31G\*, MP2/6-31+G\*, and MP2/6-311+G\* results. In addition to the geometry optimizations, scans along the OCO angle are calculated with  $R_{\text{C-Cl}}$  and  $R_{\text{C-O}}$  fixed at 3.0 and 1.143 Å, respectively. These geometric parameters are chosen for comparison to electrostatic calculations to be described below.<sup>23</sup> The results of these calculations will be discussed in Sec. IV A 3.

With respect to the  $\angle\text{OCO}$  angle in the  $\text{Cl}^-(\text{CO}_2)$  complex, two trends are apparent in the calculated results. As the size of basis set is increased for the same level of theory, the equilibrium OCO angle consistently becomes more linear. As more electron correlation is included, the  $\text{CO}_2$  distorts from linearity. The  $R_{\text{C-Cl}}$  bond length decreases as electron correlation is added, but increases as the basis set is enlarged.

The lower-level HF/4-31G\* calculation shows the greatest  $\text{CO}_2$  distortion of all of the calculations performed. While moderate levels of theory predict less distortion, the predicted  $\angle\text{OCO}$  decreases as the level of theory is improved. The MP4/6-311+G\* population analysis for the  $\text{Cl}^-(\text{CO}_2)$  cluster indicates that  $\sim 6\%$  of the total negative charge on the complex has migrated from the  $\text{Cl}^-$  anion to the  $\text{CO}_2$  molecule. The  $\text{CO}_2$  distortion is correlated with the degree of charge transfer which ranges from  $\sim 3.5\%$  to  $\sim 7\%$  depending upon the level of theory. However, distortion of the  $\text{CO}_2$  can also result purely from electrostatic effects, and the relative contributions of these two mechanisms is addressed in Sec. IV.

### 2. $\text{FCO}_2^-/\text{FCO}_2$

Both  $\text{FCO}_2^-$  and  $\text{FCO}_2$  have been investigated theoretically at various levels of *ab initio* theory. Previous geometry optimizations<sup>9</sup> of  $\text{FCO}_2^-$  have been limited to SCF calculations which do not account for electron correlation. In order to obtain more quantitative results which may be compared to the data, we performed calculations on  $\text{FCO}_2^-$  at the MP2, MP4, and QCISD (Ref. 24) levels of theory with, in some cases, larger basis sets than previously employed. The calculations were performed using the GAUSSIAN92 *ab initio* calculation package<sup>22</sup> and the results are summarized in Table V.

The results show that the F–C bond is quite long relative to other C–F bonds [i.e.,  $R_{\text{C-F}}(\text{CH}_3\text{F})=1.39$  Å]. The OCO bond angle varies by as much as  $6^\circ$  depending upon the level of theory employed. In all cases, the OCO bond angle is very near that determined for the  $\text{CO}_2^-$  anion,  $134^\circ$ .<sup>25</sup> The results also show that the  $\text{CO}_2$  bending frequency ( $\omega_2$ ) is  $720\text{--}900\text{ cm}^{-1}$ , near the  $883\text{ cm}^{-1}$  frequency observed for matrix isolated  $\text{FCO}_2^-$  by Ault.<sup>5</sup> This suggests that the matrix absorption feature would be better assigned as the  $\text{CO}_2$  bend rather than the C–F stretch ( $\omega_3$ ) which is predicted to have a significantly lower frequency. The reassignment to the  $\text{CO}_2$  bending vibration is consistent with (1) the observed isotopic shift in  $^{18}\text{O}$  substitution studies; (2) the expected increase in this  $\text{CO}_2$  bending force constant when the electron is transferred from the  $\text{F}^-$  to the  $\text{CO}_2$  LUMO; and (3) the expected low frequency C–F stretch for such a long, and relatively weak, C–F bond.

Geometry optimizations and vibrational force constant analyses for four electronic states of  $\text{FCO}_2$  ( $^2B_2$ ,  $^2A_2$ ,  $^2A_1$ , and  $^2B_1$ ) have also been performed. The results of these calculations are summarized in Table VI. Also included in the table are the results of previous calculations for the  $^2B_2$  and  $^2A_1$  electronic states of  $\text{FCO}_2$  by Francisco and co-workers.<sup>13</sup> Due to the high excitation energies found for the  $^2A_1$  and  $^2B_1$  electronic states at the MP2/6-31+G\* level of theory ( $T_e=1.5$  eV and 5.9 eV,<sup>26</sup> respectively), no calculations be-

TABLE V. *Ab initio* calculations for  $\text{FCO}_2^- \tilde{X}^1A_1$  ground state properties.

Level of theory	Energy (a.u.)	$R_{\text{FC}}$ (Å)	$R_{\text{CO}}$ (Å)	$\angle \text{OCO}$	$\omega_1$ (a1)	$\omega_2$ (a1)	$\omega_3$ (a1)	$\omega_4$ (b1)	$\omega_5$ (b2)	$\omega_6$ (b2)
HF/6-31G	-286.970 713	1.454	1.232	135.4°	1371	894	655	841	1906	602
HF/6-31+G <sup>a</sup>	-286.994 634	1.475	1.229	136.2°	1327	815	622	834	1856	585
HF/6-31+G <sup>b</sup>	-286.994 634	1.475	1.229	136.2°	1339	816	625	838	1860	587
HF/6-31+G*	-287.112 049	1.410	1.212	135.2°	1440	893	672	920	1974	638
MP2/6-31G	-287.437 503	1.563	1.261	137.1°	1226	762	526	717	1827	512
MP2/6-31+G	-287.489 520	1.664	1.253	140.7°	1181	674	390	684	1816	454
MP2/6-31G*	-287.736 034	1.478	1.236	136.4°	1338	815	585	804	1940	565
MP2/6-31+G*	-287.799 822	1.517	1.234	138.0°	1290	724	507	783	1894	535
MP2/6-311G	-287.568 112	1.595	1.253	138.2°	1202	729	485	706	1817	493
MP2/6-311+G	-287.603 201	1.677	1.247	141.3°	1170	667	275	682	1810	449
MP2/6-311G*	-287.892 138	1.486	1.225	137.2°	1326	792	564	820	1949	570
MP2/6-311+G*	-287.927 429	1.505	1.225	137.9°	1294	738	510	801	1900	550
MP4/6-31+G	-287.510 246	1.715	1.259	141.9°	...	...	...	...	...	...
MP4/6-31+G*	-287.816 161	1.539	1.238	138.5°	...	...	...	...	...	...
MP4/6-311+G*	-287.959 000	1.523	1.230	138.4°	...	...	...	...	...	...
QCISD/6-31G*	-287.740 084	1.459	1.235	135.9°	1352	845	609	819	1914	578
Experiment <sup>c</sup>	...	...	...	...	1316	883	...	...	1749	...

<sup>a</sup>Present results.<sup>b</sup>Reference 9.<sup>c</sup>Reference 5.

yond this level were performed for these states because they most likely will not contribute to the data presented here. Experimentally, Maricq *et al.*<sup>13</sup> have observed a set of absorption features between 13 000 and 17 000  $\text{cm}^{-1}$  which they assign as the  $\tilde{B}^2A_1 \leftarrow \tilde{X}^2B_2$  transition. The term value which they measure [ $T_0(^2A_1) = 1.630$  eV] agrees well with their calculated value [ $T_0(^2A_1) = 1.606$  eV]. The two remaining electronic states,  $^2B_2$  and  $^2A_2$ , are significantly affected by changes in basis set and the degree of electron correlation considered in the calculation. At the HF/6-31+G\* level of theory, the  $^2A_2$  state is predicted to be the ground state of the fluoroformyloxyl radical with the  $^2B_2$  and  $^2A_1$  states lying 0.406 and 2.74 eV above the ground state, respectively. Inclusion of electron correlation effects by either perturbative Møller–Plesset (MP2 or MP4) or CI(QCISD) methods changes the energetic ordering of the lower two states, consistently predicting the  $^2B_2$  state as the ground state.

For the  $^2A_2$  state, calculations using the MP methods leads to a more significant problem. Force constant analyses at both the MP2 and MP4 levels of theory suggest that this  $C_{2v}$  excited state species, which results from detachment of an electron from the ( $1a_2$ ) orbital of  $\text{FCO}_2^-$ , is not located at a potential minimum. Rather, the imaginary frequency calculated for the  $\nu_6$  vibrational mode ( $\text{CO}_2$  asymmetric stretch) suggests that the  $C_{2v}$  species is a transition state structure between two lower-symmetry  $^2A''$  structures. Lowering the symmetry of the molecule, the MP2/6-31+G\* calculations predict a  $C_s$  structure which lies 0.1 eV below the  $C_{2v}$  “saddle point” structure.<sup>27</sup>

By analogy with *ab initio* calculations for the  $\text{HCO}_2$  and  $\text{NO}_2$  molecules,<sup>28,29</sup> it is likely that calculations for the fluoroformyloxyl radical will be affected by the symmetry-breaking phenomenon which results from the inability of some levels of theory to describe the resonance of the electronic structure which leads to equal bond lengths (CO or

NO) in the  $\text{HCO}_2$  and  $\text{NO}_2$  radicals. For these molecules, single reference wave functions tend to localize the unpaired electron, resulting one CO (or NO) double bond and one CO (or NO) single bond rather than a symmetric  $C_{2v}$  structure. Configuration interaction calculations (QCISD) are performed to allow a more flexible description of the possible resonance structures. As shown in Table VI, the QCISD/6-31+G\* calculation predicts a  $C_{2v}$  structure which exists at a potential minimum with the vibrational frequencies given. This result is very important for the analysis of the  $\text{FCO}_2^-$  photoelectron spectrum. For comparison to the data, the  $^2B_2$  state properties are also calculated at the QCISD/6-31G\* level of theory.

#### IV. ANALYSIS AND DISCUSSION

In the following sections, we will treat the data presented above in more detail. Due to the differences in the appearance of the data, the  $\text{X}^-(\text{CO}_2)$  clusters ( $\text{X}=\text{I}, \text{Br}, \text{Cl}$ ) will be treated separately from the  $\text{FCO}_2^-$  anion. For the  $\text{X}^-(\text{CO}_2)$  data, we will discuss the most likely geometry for the anions and consider the difference in the electronic structure for the neutral complexes as one goes from I to Br to Cl. In the process, we will apply the distributed multipole analysis (DMA) model of Stone and co-workers<sup>30</sup> in order to better understand the nature of the forces between the halide anion and the  $\text{CO}_2$  molecule for the  $\text{X}^-(\text{CO}_2)$  clusters. In the case of  $\text{Cl}^-(\text{CO}_2)$ , *ab initio* calculations are compared with the experimental results. For the  $\text{FCO}_2^-$  spectrum, the electronic and vibrational structure of the fluoroformyloxyl radical is studied from a more spectroscopic viewpoint with the aid of the *ab initio* results.

TABLE VI. *Ab initio* calculations for FCO<sub>2</sub> ground and excited electronic states. All frequencies ( $\omega_i$ ) given in cm<sup>-1</sup>.

$\tilde{X} \ ^2B_2$	Energy (a.u.) <sup>c</sup>	$T_e$ (eV)	$R_{FC}$ (Å)	$R_{CO}$ (Å)	$\angle OCO$	$\omega_1$ (a1)	$\omega_2$ (a1)	$\omega_3$ (a1)	$\omega_4$ (b1)	$\omega_5$ (b2)	$\omega_6$ (b2)
UHF/6-31+G*	-286.978 331	0.41	1.291	1.218	117.8°	1722	1101	601	908	2703	633
MP2/6-31G** <sup>a</sup>	-287.619 3	0.0	1.324	1.244	117.4°	1626	1016	557	880	3401	574
MP2/6-31+G*	-287.632 652	0.0	1.331	1.245	117.8°	1585	991	546	870	3290	566
MP2/6-311+G*	-287.770 014	0.0	1.318	1.237	118.2°	...	...	...	...	...	...
MP4/6-311+G	-287.341 920	0.0	1.409	1.284	120.8°	1350	845	521	681	2125	503
QCISD/6-31G** <sup>b,c</sup>	-287.618 133	0.0	1.326	1.245	118.8°	1580	1007	537	...	...	...
Experiment <sup>a</sup>	...	0.0	...	...	...	...	...	520	...	...	...
Present results	...	0.0	...	...	...	1465 (70)	950 (70)	500 (70)	...	...	...
$\tilde{A} \ ^2A_2$											
UHF/6-31+G*	-286.993 254	0.0	1.311	1.244	124.6°	1565	1067	659	660	705	544
MP2/6-31G*	-287.584 751	d	1.337	1.248	124.8°	1531	1031	637	584	614	1397 <i>i</i>
MP2/6-31+G*	-287.602 790	d	1.346	1.248	125.3°	1499	998	630	564	604	1400 <i>i</i>
MP2/6-311G	-287.400 777	d	1.399	1.267	126.1°	1360	901	608	725	565	889 <i>i</i>
MP4/6-31+G	-287.309 680	d	1.418	1.279	126.8°	1309	868	595	714	551	646 <i>i</i>
QCISD/6-31G*	-287.602 032	0.44	1.339	1.262	125.1°	1480	1003	616	746	658	384
Present results	...	$T_0 =$ 0.579	...	...	...	1274 (40)	903 (40)	532 (40)	...	...	...
$\tilde{B} \ ^2A_1$											
UHF/6-31+G*	-286.892 389	2.74	1.350	1.222	137.0°	1272	798	679	849	1735	581
MP2/6-31G** <sup>a</sup>	-287.567 1	1.42	1.360	1.260	137.8°	1283	1048	520	742	2413	566
MP2/6-31+G*	-287.578 778	1.47	1.367	1.263	137.8°	1262	1033	611	732	2356	558
QCISD/6-31G** <sup>a</sup>	287.555 9	1.69	1.370	1.258	137.0°	...	...	...	...	...	...
Experiment <sup>a</sup>	...	$T_0 =$ 1.63	...	...	...	...	1110	610	840	2820	...
$^2B_1$											
UHF/6-31+G*	-286.755 039	6.08 <sup>c</sup>	1.287	1.322	70.0°	1893	1058	725	1616 <i>i</i>	1231	442
MP2/6-31+G*	-287.416 961	5.89	1.315	1.358	75.4°	...	...	...	...	...	...

<sup>a</sup>Reference 13.<sup>b</sup>Geometries from Ref. 12, vibrational frequencies from present work.<sup>c</sup>MP2 energies are energies obtained after annihilation of spin contamination; MP4 are the MP4SDTQ energies.<sup>d</sup>Force constant analysis indicates that geometry is not located at a potential energy minimum, but rather at a saddle point.<sup>e</sup>See Ref. 46.

## A. X=I, Br, Cl

### 1. Electron affinities and thermodynamics

From the data in Fig. 2, the most readily derived information is the electron affinity (EA) for each of the X(CO<sub>2</sub>) complexes. For Br<sup>-</sup>(CO<sub>2</sub>) and Cl<sup>-</sup>(CO<sub>2</sub>), the EA is determined using Eq. (2) for the 0–0 transition in the spectrum. EA[I(CO<sub>2</sub>)] = 3.225 ± 0.001 eV has previously been determined using higher resolution ZEKE spectroscopy.<sup>8</sup> Based upon comparison of photoelectron spectrum and ZEKE spectra of I<sup>-</sup>(CO<sub>2</sub>), the 0–0 transition for each X<sup>-</sup>(CO<sub>2</sub>) spectrum is assumed to lie at the position indicated by an arrow in Fig. 2. Using the values for the ground state origins of the spectra, the EA's of the Br(CO<sub>2</sub>) and Cl(CO<sub>2</sub>) complexes are determined to be 3.582 ± 0.017, and 3.907 ± 0.010 eV, respectively. The different error bars result from the (eKE)<sup>3/2</sup> dependence of the spectrometer resolution function.

The EA's of X(CO<sub>2</sub>) clusters can, in principle, be combined with the measured values for the X<sup>-</sup>–(CO<sub>2</sub>) binding energies to determine the X–CO<sub>2</sub> binding energy. The diagram in Fig. 4 shows that the difference in the EA's of X and X·CO<sub>2</sub> results from the difference in the  $D_0(X\text{--}CO_2)$  and

$D_0(X^-\text{--}CO_2)$  energies. The shift of the X<sup>-</sup>(CO<sub>2</sub>) spectrum to lower eKE relative to the X<sup>-</sup> spectrum is attributed to the stronger bond of the charged cluster. Figure 4 show that  $D_0(X\text{--}CO_2)$  is given by

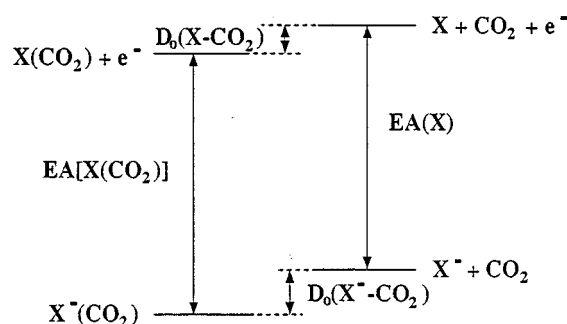


FIG. 4. Schematic diagram illustrating the thermodynamic relationships between the anionic and neutral clusters. These relationships are used to derive Eq. (4) in the text.



$$D_0(\text{X}-\text{CO}_2) = \text{EA}(\text{X}) + D_0(\text{X}^- - \text{CO}_2) - \text{EA}(\text{X} \cdot \text{CO}_2). \quad (4)$$

High pressure mass spectrometry (HPMS) clustering studies provide  $\Delta H^0$  values (at 298 K) which can be converted to  $D_0$  using the vibrational frequencies of the clusters. If the C–X stretch and bend frequencies for all the anion complexes are on the order of that measured<sup>8</sup> for the stretch in  $\text{I}^-(\text{CO}_2)$ ,  $64 \text{ cm}^{-1}$ , then the  $D_0(\text{X}^- - \text{CO}_2)$  values will be approximately 0.25 kcal/mol larger than the measured  $\Delta H_{0,1}^0(\text{X}^- - \text{CO}_2)$  values. Keesee *et al.*<sup>3</sup> measure  $\Delta H_{0,1}^0(\text{Cl}^- - \text{CO}_2) = 8.0 \pm 0.1 \text{ kcal/mol}$  ( $0.347 \pm 0.004 \text{ eV}$ ) and  $\Delta H_{0,1}^0(\text{I}^- - \text{CO}_2) = 5.6 \pm 0.1 \text{ kcal/mol}$  ( $0.243 \pm 0.004 \text{ eV}$ ). Hiraoka *et al.*<sup>4</sup> measure  $\Delta H_{0,1}^0(\text{Cl}^- - \text{CO}_2) = 7.6 \text{ kcal/mol}$  ( $0.330 \text{ eV}$ ),  $\Delta H_{0,1}^0(\text{Br}^- - \text{CO}_2) = 6.7 \text{ kcal/mol}$  ( $0.290 \text{ eV}$ ), and  $\Delta H_{0,1}^0(\text{I}^- - \text{CO}_2) = 4.7 \text{ kcal/mol}$  ( $0.204 \text{ eV}$ ). Substituting the appropriate  $D_0[\text{X}^- - (\text{CO}_2)]$  values into Eq. (14) yields providing  $D_0(\text{X}-\text{CO}_2)$  values which are quite small (0.5–1 kcal/mol) with error bars of the same order of magnitude. Thus, as expected, the Cl, Br, and I neutral complexes are very weakly bound van der Waals clusters and an accurate determination of their binding energies will require a higher resolution ZEKE investigation. Such a study of the  $\text{I}(\text{CO}_2)$  cluster found  $D_0(\text{I}-\text{CO}_2) = 0.0445 \pm 0.0036 \text{ eV}$ .<sup>8</sup>

## 2. Underlying structure

As mentioned in Sec. II, the peak widths in the  $\text{X}^-(\text{CO}_2)$  spectra are significantly broader than the experimental resolution. In addition, the peak widths of the  $\text{I}^-(\text{CO}_2)$  and  $\text{Br}^-(\text{CO}_2)$  ground state ( $^2P_{3/2}$ ) bands are broader than the excited state features. Since hot band and rotational contributions should not differ significantly between the ground and excited states other effects must account for the differing peak widths. Two effects will be addressed here which contribute to the peak widths. The first contribution, which affects the ground and excited states approximately equally, results from excitation of the X–CO<sub>2</sub> van der Waals stretch by photodetachment of the  $\text{X}^-(\text{CO}_2)$  anions. As a result of the significant difference in the interaction energies of the anion and neutral, one expects the X–CO<sub>2</sub> distance to increase upon photodetachment. While the van der Waals progression is not resolved in the data presented here due to our limited resolution, it was seen in the ZEKE spectrum of  $\text{I}^-(\text{CO}_2)$ .<sup>8</sup>

In addition to the van der Waals progressions, there is an electronic effect which contributes only to the  $^2P_{3/2}$  bands in the  $\text{I}^-(\text{CO}_2)$  and  $\text{Br}^-(\text{CO}_2)$  spectra. The correlation diagram for a closed-shell atom (Rg)/open-shell atom (X) interaction, which is analogous to that for neutral  $\text{X}(\text{CO}_2)$ , is shown in Fig. 5. The degeneracy of the  $^2P_{3/2}$  state of the halogen atom is lifted by the approach of the CO<sub>2</sub> molecule which breaks the isotropic spatial symmetry of the bare halogen atom. As seen in Fig. 5, this interaction leads to three electronic states, identified as X 1/2, I 3/2, and II 1/2 according to the projection of the total electronic angular momentum onto the symmetry axis of the cluster. The extra width of the “ground state” peak in the  $\text{I}^-(\text{CO}_2)$  spectrum results from this splitting ( $225 \text{ cm}^{-1}$ ) (Ref. 8) which is too small to be cleanly resolved in the photoelectron spectrum. However, the larger  $280 \text{ cm}^{-1}$  splitting can be observed in the  $\text{Br}^-(\text{CO}_2)$  spec-

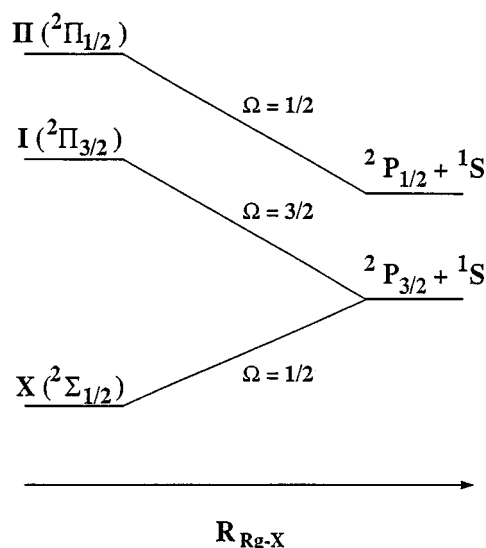


FIG. 5. Correlation diagram for an open-shell atom/closed-shell atom interaction showing the three electronic states ( $X1/2$ ,  $I3/2$ , and  $II1/2$ ) which arise from this interaction.

trum, indicating that the  $\text{Br}(\text{CO}_2)$  interaction is stronger than that of  $\text{I}(\text{CO}_2)$ . As mentioned above, the small spin–orbit splitting of the Cl atom leads to significant congestion of the  $\text{Cl}^-(\text{CO}_2)$  spectrum. Simulations in the following section provide further insight into the nature of the underlying electronic and vibrational structure for this spectrum.

## 3. Geometry and bonding

In order to analyze the vibrational structure present in the  $\text{X}^-(\text{CO}_2)$  data presented above, it is useful to have some idea of the anion geometry, particularly the site where the  $\text{X}^-$  binds to the CO<sub>2</sub>. The simplest approach is to consider the electrostatics involved. As a CO<sub>2</sub> molecule approaches the halide anion, the electrostatic interaction between the two is dominated by the charge-quadrupole interaction,

$$U_{q-\theta} = \frac{q\theta}{2R^3} (3 \cos^2 \xi - 1). \quad (5)$$

In Eq. (5),  $q = -e$  is the halide charge and  $\theta = -4.3 \times 10^{-26} \text{ esu cm}^2$  is the CO<sub>2</sub> quadrupole moment.<sup>31</sup> The negative sign of  $\theta$  indicates that the carbon atom is positively charged, relative to the two oxygen atoms. The variable,  $\xi$ , is the angle between the CO<sub>2</sub> symmetry axis and the X–C bond. According to Eq. (5), the minimum energy configuration for the halide anion separated from a rigid CO<sub>2</sub> molecule by a distance,  $R$ , occurs when  $\xi = 90^\circ$ . In a related study, Duncan and co-workers<sup>32</sup> have determined that  $\text{Mg}^+(\text{CO}_2)$ , in which CO<sub>2</sub> is complexed with a cation, has a linear geometry as predicted by Eq. (5).

The vibrational structure in the  $\text{X}^-(\text{CO}_2)$  spectra indicates that this very simple model does not fully describe the geometry of the anion clusters. Of the three CO<sub>2</sub> vibrational frequencies ( $\nu_1 = 1388 \text{ cm}^{-1}$ ;  $\nu_2 = 667 \text{ cm}^{-1}$ ;<sup>33</sup> and  $\nu_3 = 2349.2 \text{ cm}^{-1}$ ),<sup>34</sup> the spacings of the peaks in the  $\text{X}^-(\text{CO}_2)$  spectra ( $\sim 660 \text{ cm}^{-1}$  for  $\text{I}^-(\text{CO}_2)$  and  $\sim 750 \text{ cm}^{-1}$  for

$\text{Br}^-(\text{CO}_2)$  and  $\text{Cl}^-(\text{CO}_2)$  most closely match the bending frequency. This indicates that this progression is best attributed to the excitation of the  $\text{CO}_2$  bending mode of the neutral  $\text{X}(\text{CO}_2)$  complex by photodetachment of the  $\text{X}^-(\text{CO}_2)$  cluster. The excitation observed in the spectrum shows that the anion must be bent in either the anion or neutral species. As discussed in Sec. IV A 1, the neutral binding is an order of magnitude weaker than that of the anion. In a charge-quadrupole interaction, like that in  $\text{X}^-(\text{CO}_2)$ , the charge feels an attraction for the center of the quadrupole and a repulsion for ends of the quadrupole. A strong interaction of this type will distort the  $\text{CO}_2$  molecule; thus, the  $\text{CO}_2$  distortion is expected to occur in the anion.

In these complexes, the  $\text{CO}_2$  bending vibration involves primarily motion of the carbon and oxygen atoms while the halogen/halide atom remains relatively stationary. Thus it is reasonable to assume the  $\text{CO}_2$  bending modes of  $\text{X}^-(\text{CO}_2)$  and  $\text{X}\cdot\text{CO}_2$  are the same as the bending normal mode of the free  $\text{CO}_2$  molecule,  $Q_{\text{CO}_2}$ . Within this approximation, quantitative information about the  $\text{CO}_2$  distortion in the anion can be determined through a Franck-Condon analysis of the data. In photoelectron spectroscopy, the intensity of the vibrational peaks,  $I$ , are determined by the Franck-Condon factors (FCFs), as in Eq. (6),

$$I \propto v_e \cdot |\tau_e|^2 \cdot |\langle \psi_v(Q_{\text{CO}_2}) | \psi_v(Q_{\text{CO}_2}) \rangle|^2. \quad (6)$$

Here,  $\tau_e$  is the electronic transition dipole, which is assumed to be constant for a particular electronic state, and  $v_e$  is the asymptotic velocity of the detached electron.<sup>35</sup> The FCF,  $|\langle \psi_v | \psi_v \rangle|^2$ , is the spatial overlap between anion and neutral wave functions for the  $\text{CO}_2$  bending vibration. Thus, the length of the progression is determined from the displacement along the bending normal coordinate, and once this is determined, one obtains the change in the OCO bond angle upon photodetachment of  $\text{X}^-(\text{CO}_2)$ . Calculation of the FCF's results in a stick spectrum which, when convoluted with the experimental resolution function, can be compared with the experimental data.

For each spectrum, the change in OCO angle was varied to obtain the best agreement of the convoluted FCF's with the experimental peak intensities. The  $\text{CO}_2$  bending vibrational frequency is assumed to be the same in the anion and the neutral and is set to the observed experimental spacing. In Fig. 6, the Franck-Condon simulations are shown with the experimental data (circles). In the  $\text{I}^-(\text{CO}_2)$  and  $\text{Br}^-(\text{CO}_2)$  data, only the  $\text{X}(^2P_{1/2})\cdot\text{CO}_2$  state is fit for simplicity. A normal mode analysis of the optimized parameters in the simulations gives the OCO angles in  $\text{I}^-(\text{CO}_2)$  and  $\text{Br}^-(\text{CO}_2)$  of  $174.5 \pm 1.5^\circ$  and  $172.2 \pm 1.5^\circ$ , respectively, assuming the  $\text{CO}_2$  is linear in the two neutral complexes.

The congestion of the  $\text{Cl}^-(\text{CO}_2)$  spectrum precludes a similar simple treatment of the  $\text{Cl}(^2P_{1/2})\cdot\text{CO}_2$  state. Therefore, all three electronic states of the neutral cluster ( $X\ 1/2$ ,  $I\ 3/2$ , and  $II\ 1/2$ ; see Sec. IV A 2) are included in the simulation and convoluted together for comparison with the data. The same normal coordinate displacement is used for all three states. The total intensity of the  $II\ 1/2$  state is varied with respect to the other two states which are given equal

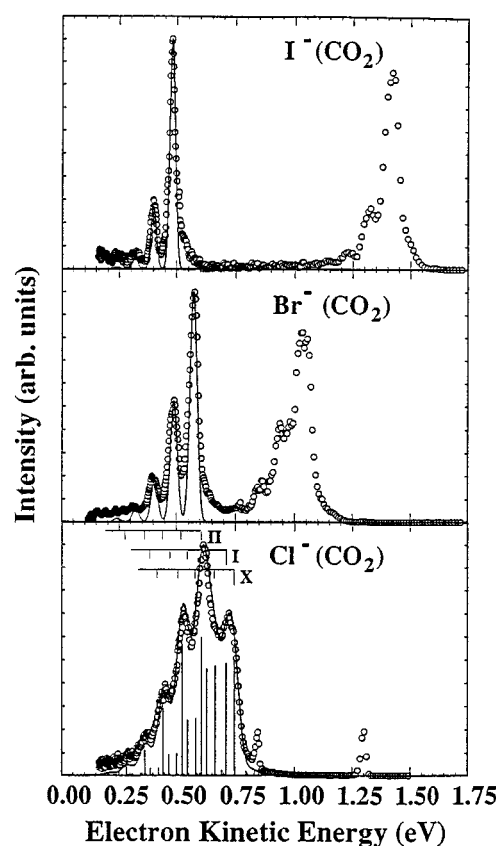


FIG. 6. Photoelectron spectra (circles) of  $\text{I}^-(\text{CO}_2)$ ,  $\text{Br}^-(\text{CO}_2)$ , and  $\text{Cl}^-(\text{CO}_2)$  and Franck-Condon simulations convoluted with the experimental resolution (solid line) and with a stick spectrum for  $\text{Cl}^-(\text{CO}_2)$ .

intensities. In the simulations, the vibrational frequencies, assumed to be equal for all three states, are also varied as are the splittings between the  $X$ ,  $I$ , and  $II$  states. The peaks are convoluted with the experimental resolution plus an additional 30 meV Gaussian, to account for unresolved van der Waals progressions, by comparison with the other  $\text{X}^-(\text{CO}_2)$  spectra. In Fig. 6, the  $\text{Cl}^-(\text{CO}_2)$  experimental spectrum is superimposed upon two Franck-Condon simulations. One has been convoluted to the experimental resolution function and the other is a stick spectrum which shows individual transitions more clearly. The parameters determined from the fit indicate that the vibrational frequency is  $\sim 700 \pm 50\text{ cm}^{-1}$ . The splitting between the  $X\ 1/2$  and  $I\ 3/2$  states is 35 meV and the  $I\ 3/2-II\ 1/2$  splitting is 104 meV. The larger uncertainties for these values, 10 meV, are due to the congestion of the transitions. As a comparison, Aquilanti and co-workers determine the  $X-I$  and  $I-II$  splittings for  $\text{Cl-Ar}$  (4 and 108 meV),  $\text{Cl-Kr}$  (8 and 107 meV),  $\text{Cl-Xe}$  (18 and 107 meV), and  $\text{Cl-CH}_4$  (16 and 106 meV) using beam scattering methods.<sup>36</sup> The larger splittings for the  $\text{Cl-CO}_2$  are reasonable since the  $\text{CO}_2$  quadrupole leads to a stronger intermolecular interaction than is present in the systems studied by Aquilanti. From the optimized change in normal coordinate, the OCO bond angle in  $\text{Cl}^-(\text{CO}_2)$  is determined to be  $169.2 \pm 2.5^\circ$ .

The simulations show that the  $\text{CO}_2$  molecule is distorted in the  $\text{X}^-(\text{CO}_2)$  anions and that the distortion increases as the

halide decreases in size. There are two possible mechanisms by which this distortion can occur. First, there may be partial charge transfer from the halide to the CO<sub>2</sub>. It is well known that CO<sub>2</sub> is stabilized by distortion from linearity when an electron is placed in the LUMO ( $2\pi_u^*$ ) orbital. The OCO angle,  $\alpha$ , is 134° in metastable CO<sub>2</sub><sup>-</sup> (Ref. 25) and 122° in the CO<sub>2</sub>[ $\tilde{A}^1B_2(\Delta_u)$ ] excited state,<sup>37</sup> which is formed by promotion of an electron from the ( $1\pi_g$ ) HOMO orbital to the ( $4a_1$ ) component of the ( $\pi_u^*$ ) LUMO. Distortion of the CO<sub>2</sub> can also come about from electrostatic effects resulting from the attractive X<sup>-</sup>/C and repulsive X<sup>-</sup>/O interactions. In order to determine the relative importance of these two mechanisms, it is useful to determine the extent of distortion due to the electrostatic interaction alone. This is the objective of the following section.

#### 4. Electrostatic models

*Ab initio* calculations for the Cl<sup>-</sup>(CO<sub>2</sub>) complex, discussed in Sec. III B 1, predict a bent CO<sub>2</sub> subunit but provide little insight into the mechanism for this distortion. Therefore, two electrostatic calculations, which neglect quantum mechanical charge exchange between X<sup>-</sup> and CO<sub>2</sub>, are presented. These calculations attempt to address the bonding in the I<sup>-</sup>, Br<sup>-</sup>, and Cl<sup>-</sup> clusters and to determine how their energies change as a function of the OCO angle.

The electrostatic calculations differ in their treatment of the CO<sub>2</sub> molecule. The simplest electrostatic model (EM) assumes the quadrupole of the CO<sub>2</sub> can be modeled as three point charges, one on each of the three atoms. In the other model, the CO<sub>2</sub> electrostatic properties are determined using the distributed multipole analysis (DMA) of Stone and co-workers.<sup>30</sup> The electrostatic properties of the CO<sub>2</sub> molecule, in both models, are determined by *ab initio* calculations using the CADPAC *ab initio* package.<sup>38</sup> The energy and electrostatic properties of the CO<sub>2</sub> molecule are determined at the HF/6-31+G\* level of theory at several  $\theta_{OCO}$  angles between 165° and 179°. The CO bond length is held at 1.1433 Å, the value determined in a geometry optimization of CO<sub>2</sub> at the HF/6-31+G\* level of theory. Experiment determines the CO<sub>2</sub> bond length to be 1.158 Å.<sup>39</sup>

Once the electrostatic properties of the CO<sub>2</sub> are calculated, the X<sup>-</sup>-CO<sub>2</sub> interaction energy is calculated using classical electrostatic interaction formulas.<sup>40</sup> The halide is treated as a polarizable negative charge located at the distance from the halide to the CO<sub>2</sub> center of mass,  $R_{X-CO_2}$ , along the  $C_{2v}$  symmetry axis of the complex. The polarizability of the halides, taken from Sangachin *et al.*,<sup>41</sup> are 3.82, 5.16, and 7.53 Å<sup>3</sup> for Cl<sup>-</sup>, Br<sup>-</sup>, and I<sup>-</sup>, respectively. Although the polarizability of the halides is included in the calculation to account for induction forces, the effect of the induction forces (quadrupole-induced dipole, etc.) on the energies calculated at different geometries is found to be relatively insignificant (<1%). Another induction term, the X<sup>-</sup>-CO<sub>2</sub> charge-induced dipole term, will simply add a constant factor as a function of the CO<sub>2</sub> angle because the CO<sub>2</sub> polarizability will not vary significantly over the geometry changes considered. For this reason it is not included in the model.

The EM model uses the partial charges of the CO<sub>2</sub> atoms output by CADPAC at each  $\theta_{OCO}$  calculated. These charges are substituted into Eq. (7) to determine the electrostatic interaction energy for each value of  $\theta_{OCO}$ ,

$$U_{elec} = \sum_a \frac{q_x q_a}{r_{xa}} + \text{induction terms.} \quad (7)$$

In Eq. (7),  $q_x = -e$  is the halide charge,  $q_a$  is the partial charge of atom  $a$  in the CO<sub>2</sub> molecule, and  $r_{xa}$  is the distance between the halide and atom  $a$  at a particular OCO bond angle. In all of the electrostatic calculations, the distance between X<sup>-</sup> and the CO<sub>2</sub> center-of-mass,  $R_{X-CO_2}$ , is held constant with respect to the X<sup>-</sup> position as the OCO angle is changed. One specific value of  $R_{X-CO_2}$  is chosen based upon our previous ZEKE results for I<sup>-</sup>(CO<sub>2</sub>). The other  $R_{X-CO_2}$  values are chosen to cover the range which might be expected to occur in the X<sup>-</sup>(CO<sub>2</sub>) complexes (i.e., 2.5 Å <  $R_{X-CO_2}$  < 4.0 Å).

In addition to the electrostatic interactions, the CO<sub>2</sub> distortion energy must be considered. This distortion energy is included in the *ab initio* calculation of the total energy of the CO<sub>2</sub> molecule. At each angle the calculated energy of the CO<sub>2</sub> molecule,  $U_{HF}^{CO_2}(\varphi)$ , is added to the calculated electrostatic potential energy to obtain the total energy,

$$U_{tot}(\varphi) = U_{HF}^{CO_2}(\varphi) + U_{elec}(\varphi). \quad (8)$$

Equation (8) represents the sum of two competing terms. The first term, describing the energy of the free CO<sub>2</sub> molecule, favors  $\theta_{OCO} = 180^\circ$  while the second term, describing the interaction between the X<sup>-</sup> and CO<sub>2</sub>, drives a distortion to  $\theta_{OCO} < 180^\circ$ . The magnitude of this distorting force is dependent upon  $R_{X-CO_2}$ . In the following discussion, the minima of all of the  $U_{tot}(\varphi)$  functions calculated using Eq. (8) are offset to zero (or another appropriate value) for ease of comparison.

A more sophisticated treatment of the electrostatic forces is based upon a DMA analysis of the CO<sub>2</sub> molecule. Stone,<sup>30</sup> Buckingham,<sup>42</sup> and their co-workers have successfully used the distributed multipole analysis to calculate the equilibrium geometries of several van der Waals complexes. They find that the structures of the van der Waals complexes can usually be calculated by accurately determining the electrostatic properties of the molecules which comprise the clusters. The DMA approach differs from the simpler electrostatic model (EM) in that it considers the electrostatic fields of the electron charge distribution within each monomer. This results in a more detailed electrostatic field for each monomer than considered in the EM calculations. These calculations have previously been used for neutral clusters composed of rigid molecular subunits. Our application represents an extension of their method because we allow the CO<sub>2</sub> molecules to distort as part of the energy optimization of the charged cluster. In the limit that the X<sup>-</sup>(CO<sub>2</sub>) complexes are governed by purely electrostatic interactions, the DMA approach should predict geometries near those which we observe experimentally.

We now summarize the procedure followed during the DMA calculations. At each  $\theta_{\text{OCO}}$ , an *ab initio* wave function for  $\text{CO}_2$ , calculated using the Hartree–Fock self-consistent field method (SCF), is analyzed to produce a charge density map. This map includes effects from both electronic and nuclear charges. Then, a set of points is defined within the  $\text{CO}_2$  molecular framework which are used as centers for electrostatic multipole expansions. Five expansion centers are used in the calculations; one on each atom and one at each CO bond midpoint. The expansion coefficients are adjusted to give a best fit to the quantum mechanically determined charge distribution. At the HF/6-31+G\* level of theory, the  $\text{CO}_2$  quadrupole is calculated to be  $-4.05 \times 10^{-26}$  esu  $\text{cm}^2$  which is slightly lower than but in reasonable agreement with the experimentally determined value of  $-4.3 \times 10^{-26}$  esu  $\text{cm}^2$ .<sup>31</sup>

In these calculations, the multipole expansion includes terms through hexadecapole at each expansion center. Once the multipoles are calculated, the energy of interaction between the halide and the  $\text{CO}_2$  is calculated from

$$U_{\text{elec}}(\varphi) = \sum_{aA} \sum_{bB} U_{ab}(\varphi), \quad (9)$$

where

$$(4\pi\epsilon_0)U_{ab}(\varphi) = \frac{q^a q^b}{R} - R_\alpha (\mu_\alpha^b q^a - \mu_\alpha^a q^b) / R^3 + (3R_\alpha R_\beta - R^2 \delta_{\alpha\beta}) (q^a \theta_{\alpha\beta}^b + q^b \theta_{\alpha\beta}^a - 3\mu_\alpha^a \mu_\beta^b) / 3R^5 + \dots, \quad (10)$$

$\mathbf{R}$  is the vector between site  $a$  in the  $A$  monomer and site  $b$  in the  $B$  monomer. In our case,  $A$  is the halide anion, the only electrostatic component of which is the charge,  $q^a$ , and  $B$  is the  $\text{CO}_2$  molecule. In this expression,  $q$ ,  $\mu$ , and  $\theta$  represent the charge, dipole, and quadrupole moments at the sites  $a$  or  $b$ . The angle  $\varphi$  is the XCO angle of the complex. Since  $A$  only has a charge, Eq. (10) simplifies significantly to give

$$(4\pi\epsilon_0)U_{ab} = \frac{q^a q^b}{R} - R_\alpha (\mu_\alpha^b q^a) / R^3 + \dots. \quad (11)$$

Additionally, at each  $\theta_{\text{OCO}}$ , terms for the induction forces, discussed above, are included [but not shown in Eq. (10) or Eq. (11)]. These include terms which account for the induction effects of the  $\text{CO}_2$  multipoles, through the quadrupole, at each geometry considered. As the  $\text{CO}_2$  bends, the dipole which forms becomes increasingly attracted to the negative charge of the halide atom, but the induction effects remain quite small. As in the EM calculations, Eq. (8) is used to calculate the total energy,  $U_{\text{tot}}(\varphi)$ , by including the calculated Hartree–Fock energy of the  $\text{CO}_2$  molecule. The calculations are performed at the same  $R_{\text{X-CO}_2}$  distances chosen for the EM calculations.

A comparison of the electrostatic calculations is shown in Fig. 7, where  $R_{\text{X-CO}_2} = 3.8 \text{ \AA}$ , the bond length determined for the  $\text{I}^-(\text{CO}_2)$  complex from the analysis of the ZEKE spectrum<sup>8</sup> for this complex. The plot shows the total energy,  $U_{\text{tot}}(\varphi)$  as a function of the XCO bond angle,

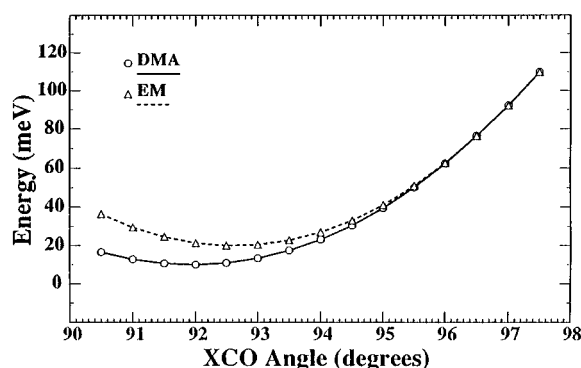


FIG. 7. Plot of normalized  $\text{X}^-(\text{CO}_2)$  energy as function of the XCO angle for the electrostatic calculations described in the text. The energies of the minima in the curves are separated by 10 meV for clarity.

$\varphi (= \pi - \frac{1}{2}\theta_{\text{OCO}})$ , over the range  $90^\circ$  to  $98^\circ$ . For all of the calculations, a minimum in the energy of the complex occurs at a geometry away from the linear  $\text{CO}_2$  configuration. At this  $R_{\text{X-CO}_2}$  distance, the calculations predict approximately the same distortion of the  $\text{CO}_2$ ,  $\angle\text{OCO} \sim 175^\circ$ – $176^\circ$ . These agree well with the experimentally determined  $\angle\text{OCO} = 174.5 \pm 1.5^\circ$  for  $\text{I}^-(\text{CO}_2)$ .

If  $R_{\text{X-CO}_2}$  is decreased, greater  $\theta_{\text{OCO}}$  distortion occurs. Calculations at four different  $R_{\text{X-CO}_2}$  distances are shown in Fig. 8. The calculated minimum energy OCO angles,  $\theta_{\text{min}}$ , for the calculations (Table VII) are determined from the derivatives of a polynomial fit to the calculated data points. At each  $R_{\text{X-CO}_2}$  distance, DMA predicts less  $\text{CO}_2$  distortion than EM. In principle, the DMA method should provide a more accurate description than EM because the increased flexibil-

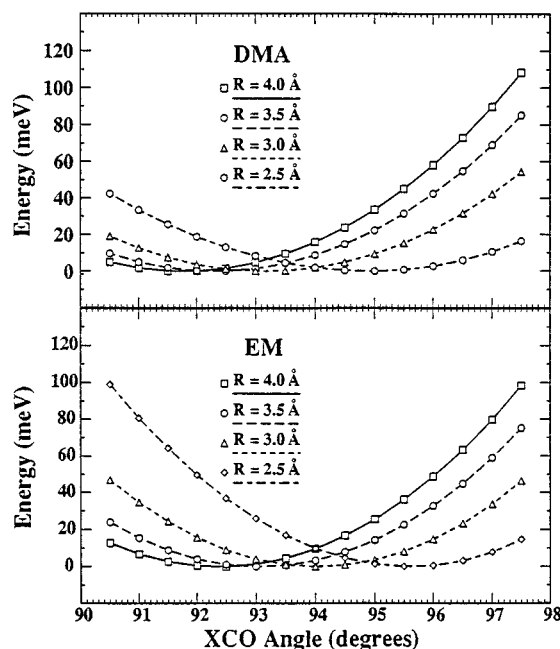


FIG. 8. Results of distributed multipole analysis (DMA) and simple electrostatic (EM) calculations of energy of the  $\text{X}^-(\text{CO}_2)$  clusters as a function of the XCO bond angle. See text for calculation details.

TABLE VII. DMA analysis results from optimum OCO angle in  $X^-(CO_2)$ .

$R_{X-C}$ (Å)\calculation	EM	DMA
2.5	168.8	170.3
3.0	172.0	173.7
3.5	174.0	175.7
4.0	175.4	176.4

ity of the multipole expansion allows for a better description of the potential field of the  $CO_2$  molecule. The increasing deviation between the EM and DMA models as  $R_{X-CO_2}$  decreases may result because the local potential becomes more important at the smaller  $X^--CO_2$  distances, where the DMA calculation more accurately accounts for the local potential field.

While the  $R_{X-CO_2}$  distances for the  $Cl^-(CO_2)$  and  $Br^-(CO_2)$  clusters have not been experimentally determined, a comparison can be made between the electrostatic calculations, the *ab initio* results for  $Cl^-(CO_2)$  and the Franck-Condon analysis of the  $Cl^-(CO_2)$  photoelectron spectrum. The MP2 and MP4 geometry optimizations for  $Cl^-(CO_2)$  suggest that the  $R_{C-Cl}$  distance is  $\sim 3.0$  Å. Comparison of the MP2 potential scan along  $\theta_{OCO}$  with the electrostatic calculations for  $R_{X-C}=3.0$  Å is shown in Fig. 9. In these electrostatic calculations, no center of mass correction is made so that the same  $R_{X-C}$  distances are used at each  $\theta_{OCO}$  in the electrostatic calculations and the MP2 potential surface scan. Excellent agreement is found with the EM calculation. The DMA expansion predicts less  $CO_2$  distortion which does not agree quite as well with the *ab initio* results, although the discrepancy in  $\theta_{min}$  is only  $1^\circ$  ( $171^\circ$  vs  $172^\circ$ ). Both values are close to experimental result of  $169.2 \pm 2.5^\circ$  for  $Cl^-(CO_2)$ .

Overall, the comparison of the EM and DMA models to experiment and *ab initio* calculations shows that electrostatic interactions alone are the primary cause of the  $CO_2$  distortion in  $X^-(CO_2)$  anions. The contribution of charge transfer to this distortion appears to be relatively minor. The dominant role of electrostatic interactions in the  $X^-(CO_2)$  clusters is consistent with the results of high pressure mass spectrometry results<sup>3,4</sup> where the sequential binding energies for  $X^-(CO_2)_n$  clusters are relatively constant for the first few  $CO_2$  molecules which attach to the halide. However, there

are some indications that charge transfer does occur and play a role in the anion geometry. For example, the DMA model predicts slightly more linear OCO bond angles in  $I^-(CO_2)$  and  $Cl^-(CO_2)$  than are experimentally observed; the additional distortion may be from charge transfer.

Another possible indication of charge transfer comes from comparing the experimental and *ab initio* values for  $R_{X-CO_2}$  with the ionic radii or van der Waals radii of the components of the  $X^-(CO_2)$  complexes. As a simple approximation, we choose to sum the ionic radius of the halide ( $I^- = 2.20$  Å;  $Br^- = 1.96$  Å;  $Cl^- = 1.81$  Å) with the van der Waals radius of a carbon atom ( $\sim 1.45$  Å) to approximate a “hard sphere”  $R_{X-C}$  distance. The ionic and van der Waals radii of the halides are very similar. Doing so, we find  $R_{X-C}$  distances of 3.65, 3.41, and 3.26 Å for  $X=I$ ,  $Br$ , and  $Cl$ , respectively. However, the hard sphere distance for  $I^-(CO_2)$  is smaller than the observed distance (i.e., 3.65 Å vs 3.77 Å),<sup>43</sup> while for  $Cl^-(CO_2)$ , it is larger than the *ab initio* result (3.26 Å vs 3.0 Å). This trend is consistent with increasing charge transfer from the  $X^-$  to the  $CO_2$  as the halide is changed from  $I^-$  to  $Cl^-$ ; recall that our highest level *ab initio* calculation for  $Cl^-(CO_2)$  predicts about 7% charge transfer.

## B. $FCO_2^-$

### 1. Spectroscopy and Franck-Condon analysis

As discussed in Sec. III A 1, the  $FCO_2^-$  photoelectron spectrum (Fig. 3) contains contributions from photodetachment transitions to two different  $FCO_2$  electronic states. The states of  $FCO_2$  which may be observed by this technique are those which can be formed by one-electron photodetachment of  $FCO_2^-$ . Removal of an electron from any of the four highest-lying occupied molecular orbitals of the  $FCO_2^-$   $\tilde{X}^1A_1$  ground state [ $\dots(2b_1)^2(8a_1)^2(5b_2)^2(1a_2)^2$ ] will lead to the formation of the  $^2A_2$ ,  $^2B_2$ ,  $^2A_1$ , and  $^2B_1$  electronic states of the  $FCO_2$  radical in  $C_{2v}$  symmetry. The  $1a_2$ ,  $5b_2$ , and  $8a_1$  orbitals are shown in Fig. 10. The assignment of the electronic states observed in the spectrum is assisted by *ab initio* calculations and previous observations for  $FCO_2$  and other isoelectronic molecules.

The QCISD/6-31G\* *ab initio* calculations predict the  $^2B_2$  state to be the ground state lying 0.437 and 1.692 eV below the  $^2A_2$  and  $^2A_1$  electronic states, respectively. As mentioned earlier, the  $^2A_1$  and  $^2B_1$  states are not accessible at a photodetachment energy of 5.822 eV. In accord with these results, the progression beginning at peak A is assigned to transitions to the  $\tilde{X}^2B_2$  ground state. This agrees with the previous assignment of the  $\tilde{B}^2A_1 \leftarrow \tilde{X}^2B_2$  absorption by Maricq *et al.*<sup>13</sup> The irregular set of peaks beginning at peak K and extending to lower eKE is assigned to the  $\tilde{A}^2A_2$  state. Weaver *et al.*<sup>44</sup> found that the lowest-lying excited state of the isoelectronic  $D_{3h}$   $NO_3$  molecule is the doubly degenerate  $^2E''$  state, which lies  $0.868 \pm 0.014$  eV above the  $^2\tilde{A}_2'$  ground state. This is consistent with the state ordering for  $FCO_2$  since the  $D_{3h}$   $^2E''$  state correlates to the  $C_{2v}$   $^2B_1$  and  $^2A_2$  states and the  $^2\tilde{A}_2'$  state correlates to the  $^2B_2$  state.

Further support for these assignments is obtained through a Franck-Condon analysis of the vibrational features observed in the spectra of both electronic states. For the

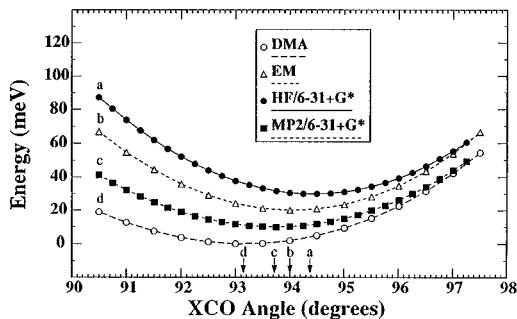


FIG. 9. Comparison of electrostatic calculations using  $R_{X-C}=3.0$  Å with results of *ab initio* calculations of the energy of the  $Cl^-(CO_2)$  complex as a function of the XCO bond angle.

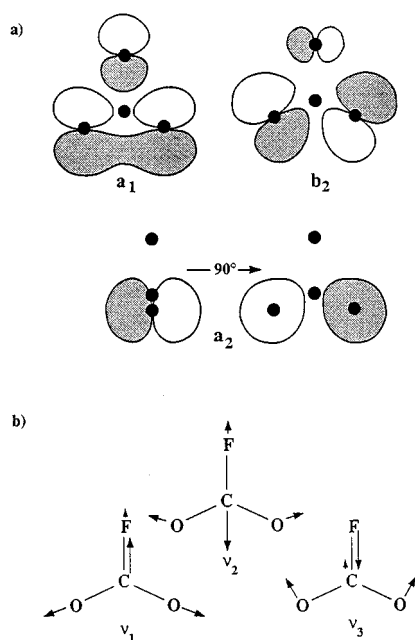


FIG. 10. Relevant molecular orbitals (a, top) and vibrational normal coordinates (b, bottom) for  $\text{FCO}_2^-$ . MOs are based upon the results of a QCISD/6-31G\* *ab initio* calculation.

$\tilde{X}^2B_2$  ground state, the values of  $\omega_e = 485 \text{ cm}^{-1}$  and  $x_e\omega_e = 2 \text{ cm}^{-1}$  determined from a least squares analysis of the peak positions A–J agree marginally with the  $\nu_3'' = 520 \text{ cm}^{-1}$  value determined from hot bands in the absorption data.<sup>13</sup> Similar agreement is found with the calculated  $\nu_3$  frequency (Table VI). However, simulations of the spectrum, discussed below, reveal that the peaks in this progressions are *not* solely attributable to a single progression in the  $\nu_3$  vibrational mode.

Due to symmetry, photodetachment of a negative ion primarily results in the excitation of totally symmetric vibrational modes in the neutral. Shown in Fig. 10(b) are the three symmetric modes of  $\text{FCO}_2$ ; the C–F stretch, C–O stretch, and CO<sub>2</sub> bend. The degree to which each of these modes are is determined by the difference in geometries and force constants of the  $\text{FCO}_2^-$  anion and the  $\text{FCO}_2$  radical. In terms of molecular orbitals, Fig. 10 shows that the removal of an electron from either the ( $5b_2$ ) or the ( $1a_2$ ) orbital of  $\text{FCO}_2^-$  will lead to a relatively smaller OCO angle for the neutral  $\text{FCO}_2$  radical. The *ab initio* calculations (Tables V and VI) suggest that all three modes will be excited for both the  $^2B_2$  and  $^2A_2$  states because the  $\text{FCO}_2^-$  and  $\text{FCO}_2$  geometries are quite different.

In Sec. IV A 3, the CO<sub>2</sub> distortion in the  $\text{X}^-(\text{CO}_2)$  clusters was determined using a Franck–Condon analysis. By assuming a CO<sub>2</sub> to be linear in the  $\text{X}(\text{CO}_2)$  neutral, the distortion of the CO<sub>2</sub> in the anion was readily determined. In the case of the  $\text{FCO}_2^-$  spectrum, we have no *a priori* knowledge of either the anion or neutral geometry. However, in order to learn more about the geometry changes that occur upon photodetachment, one can compare the experimental photoelectron spectrum to simulations based upon the *ab initio* results presented in Sec. III B 2.

The *ab initio* calculations yield a complete set of force constants in addition to the geometries discussed earlier. By standard matrix methods,<sup>45</sup> the *ab initio* force constants are used to convert the calculated geometry difference between the anion and neutral into displacements,  $\Delta Q$ , along each neutral normal mode. The resultant  $\Delta Q$  values are used as input for the calculation of Franck–Condon overlap between  $\text{FCO}_2^-$  and  $\text{FCO}_2$ . The Franck–Condon principle determines the photodetachment transition intensities,  $I$ , according to Eq. (12),

$$I = v_e \cdot |\tau_e|^2 \cdot \prod_{i=1}^6 |\langle \psi_{v_i'}(Q_i) | \psi_{v_i''}(Q_i) \rangle|^2. \quad (12)$$

As in Eq. (3),  $v_e$  is the asymptotic velocity of the detached electron and  $\tau_e$  is the electronic transition dipole. The major approximation of this analysis is that the vibrational normal modes of the anion and neutral are separable and parallel (i.e., no Duschinsky rotation), so for the simulation of each electronic band, force constants for the appropriate neutral state are used for the anion as well. Unlike Eq. (3), the “multidimensionality” of the problem leads to combination bands which are calculated as a product of Franck–Condon factors for each mode. The Franck–Condon factor,  $|\langle \psi_{v_i'} | \psi_{v_i''} \rangle|^2$ , as before, is related to the spatial overlap of the vibrational wave functions for the  $i$ th mode of the anion,  $\psi_{v_i''}$ , and neutral,  $\psi_{v_i'}$ . The resultant stick spectrum is convoluted with the experimental resolution function plus an additional 10 meV Gaussian to account for space-charge effects and rotational contours for comparison with the experimental data.

For the  $\tilde{X}^2B_2$  ground state, a Franck–Condon analysis using the QCISD/6-31G\* geometries and force constants<sup>46</sup> for  $\text{FCO}_2^-$  and  $\text{FCO}_2$  leads to the simulations shown in Fig. 11. The stick spectrum shows that all three symmetric vibrational modes are moderately excited upon photodetachment of  $\text{FCO}_2^-$ . However, when the FCF’s are convoluted with the experimental resolution, Fig. 11, a long series of peaks results which resembles the ground state spectrum of  $\text{FCO}_2$ . Since the three symmetric vibrational frequencies are nearly multiples of  $\sim 500 \text{ cm}^{-1}$ , the individual peaks for each progression are not resolved, but rather convoluted into a progression which might easily be interpreted as a progression in a single vibrational mode peaking at  $v' = 7$ . In fact, the Franck–Condon analysis indicates that for the  $\nu_1$ ,  $\nu_2$ , and  $\nu_3$  modes, the most intense transitions occur at  $v_1' = 1$ ,  $v_2' = 1$ , and  $v_3' = 2$ , respectively.

The significant amount of vibrational structure in the spectrum of the  $\tilde{A}^2A_2$  state, beginning at peak K, suggests that more than one vibrational mode is excited upon photodetachment of  $\text{FCO}_2^-$  to the first excited state of  $\text{FCO}_2$ . However, better separation of the vibrational frequencies results in a less convoluted spectrum as compared to the ground state. Using the QCISD/6-31G\* optimized parameters for  $\text{FCO}_2^-$  and the  $\text{FCO}_2^2A_2$  state, the Franck–Condon analysis produces a simulation of the excited state band, shown in Fig. 12, which agrees remarkably well with observed spectral profile and spacings. As indicated in Fig. 12, all three totally symmetric vibrational modes are excited upon photo-

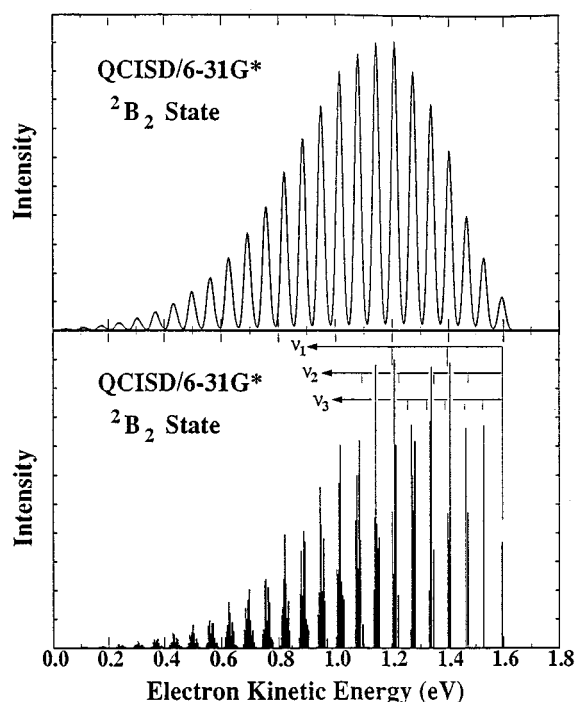


FIG. 11. Franck-Condon simulations for the  $\text{FCO}_2 \tilde{X}^2B_2 \leftarrow \text{FCO}_2^- \tilde{X}^1A_1$  photodetachment process predicted by QCISD/6-31G\* calculated geometries and force constants for anion and neutral. The Franck-Condon factors are convoluted with the experimental resolution in the top frame while the stick spectrum is shown at bottom. The simulations show that the experimentally observed progression represents moderate excitation of *all three* totally symmetric vibrational modes upon photodetachment of  $\text{FCO}_2^-$ .

detachment. The agreement between the experimental photoelectron spectrum and the *ab initio* simulations indicates that the QCISD/6-31G\* calculated results are reasonably accurate.

The *ab initio* simulations serve as a starting point to fit the spectrum within the Franck-Condon approximation. Shown in Fig. 13 is a best fit simulation of the data assuming that peaks A and K represent the origins of the  $\tilde{X}^2B_2$  and  $\tilde{A}^2A_2$  states of the  $\text{FCO}_2$  radical, respectively. The simulation was generated beginning with those shown in Figs. 11

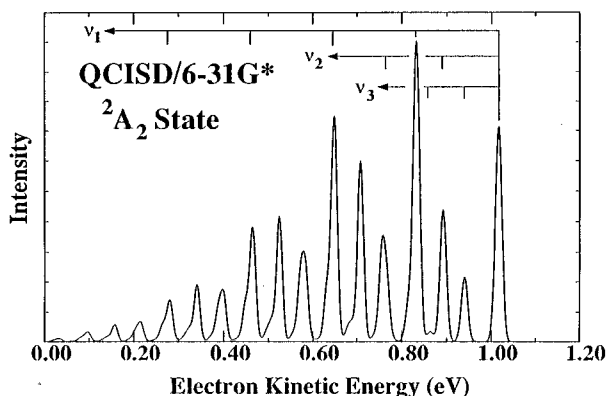


FIG. 12. Franck-Condon simulation for the  $\text{FCO}_2 \tilde{A}^2A_2 \leftarrow \text{FCO}_2^- \tilde{X}^1A_1$  photodetachment process predicted by QCISD/6-31G\* calculated geometries and force constants for anion and neutral.

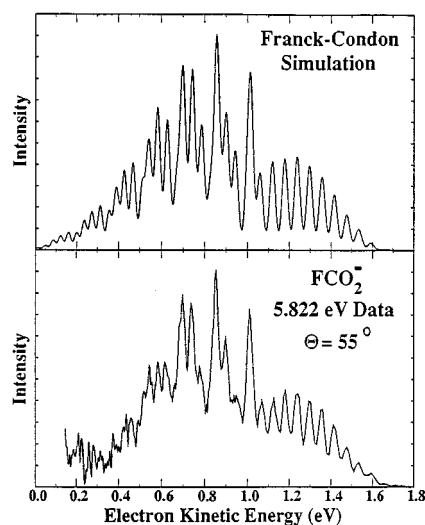


FIG. 13. Franck-Condon simulation (top) for both the  $\text{FCO}_2 \tilde{X}^2B_2 \leftarrow \text{FCO}_2^- \tilde{X}^1A_1$  and the  $\text{FCO}_2 \tilde{A}^2A_2 \leftarrow \text{FCO}_2^- \tilde{X}^1A_1$  photodetachment transitions in which the normal coordinate displacements and vibrational frequencies have been adjusted to obtain the best agreement with the experimental data (bottom).

and 12 and adjusting the changes in normal coordinates and the neutral vibrational frequencies to obtain the best agreement with the experimental peak intensities and shapes. The  $\text{FCO}_2^-$  frequencies employed are also adjusted in the simulation at a vibrational temperature of 300 K. The optimized values (Table VIII) do not differ significantly from the matrix values determined by Ault.<sup>5</sup> In the case of the CO symmetric stretch of the  $\text{FCO}_2 \tilde{A}^2A_2$  excited state, a Morse potential with  $\omega_e = 1320 \text{ cm}^{-1}$  and  $x_e \omega_e = 8 \text{ cm}^{-1}$  was used to match the anharmonicity observed for that mode in the spectrum.

Given the normal coordinate displacements, we can determine the geometries of the neutral states if we assume the *ab initio*  $\text{FCO}_2^-$  geometry is correct. In this analysis, the signs of the normal coordinate displacements are chosen to be consistent with those predicted by the *ab initio* force constants and geometries. Projection of the optimized normal coordinate displacements onto the raw *ab initio* transformation matrices provides the geometries of the  $\tilde{X}^2B_2$  and  $\tilde{A}^2A_2$  states of the  $\text{FCO}_2$  radical. The geometries which result from this analysis are given in Table VIII. The agree-

TABLE VIII. Optimized parameters for Franck-Condon simulation of the  $\text{FCO}_2^-$  photoelectron spectrum.

State	$\text{FCO}_2 \tilde{X}^2B_2$	$\text{FCO}_2 \tilde{A}^2A_2$	$\text{FCO}_2^- \tilde{X}^1A_1$
$T_0$ (eV)	0.0	0.576	0.0
$\omega_1$ ( $\text{cm}^{-1}$ )	1465 (70)	1310 (40)	1399
$x_{11}\omega_1$ ( $\text{cm}^{-1}$ )	0.0	8.0 (4)	0.0
$\omega_2$ ( $\text{cm}^{-1}$ )	950 (70)	920 (40)	899
$\omega_3$ ( $\text{cm}^{-1}$ )	500 (70)	577 (40)	596
$R_{\text{FC}}$	1.38 Å <sup>a</sup>	1.33 Å <sup>b</sup>	1.459 Å <sup>c</sup>
$R_{\text{CO}}$	1.23 Å <sup>a</sup>	1.26 Å <sup>b</sup>	1.235 Å <sup>c</sup>
$\theta_{\text{OCO}}$	119° <sup>a</sup>	125° <sup>b</sup>	135.9° <sup>c</sup>

<sup>a</sup>MP2/6-31+G\*  $\tilde{X}^2B_2$  force constants used.

<sup>b</sup>QCISD/6-31+G\*  $\tilde{A}^2A_2$  force constants used.

<sup>c</sup>Values fixed to those calculated at the QCISD/6-31G\* level of theory.

ment with the *ab initio* values (i.e., the QCISD results in Table VI) is excellent for the  ${}^2A_2$  state and reasonably good for the ground state. Of course, the accuracy of the neutral geometries determined from this Franck–Condon analysis is dependent upon the accuracy of the anion geometry and the neutral force constant matrices, as well as the simplifications made in the analysis (i.e., separable and parallel modes). However, the overall agreement of the calculated and fit neutral geometries further supports the assignments.

## 2. Electron affinity and thermochemistry

The EA of  $\text{FCO}_2$  is readily calculated as the difference between the photon energy and the eKE of the 0–0 transition using Eq. (2). Although the intensity of peak A is quite low, the Franck–Condon simulations in the previous section support the assignment of this feature as the 0–0 transition, and this yields  $\text{EA}(\text{FCO}_2) = 4.277 \pm 0.030$  eV. The sizable uncertainty for the experimental electron affinity results from the high eKE of peak A combined with the uncertainty associated with the necessary space-charge correction. The MP2/6-31+G\* and MP2/6-311+G\* calculations predict  $\text{EA}(\text{FCO}_2)$  values (4.549 and 4.295 eV, respectively) near the experimentally determined value. Calculations using basis sets without diffuse functions underestimate  $\text{EA}(\text{FCO}_2)$  significantly [i.e.,  $\text{EA}(\text{FCO}_2) = 3.176$  and  $3.319$  eV at the MP2/6-31G\* and QCISD/6-31G\* levels, respectively], illustrating the importance of diffuse functions for the accurate calculations of anion energies.

With our value for  $\text{EA}(\text{FCO}_2)$ , it is possible to determine the value of  $D_0(\text{F}–\text{CO}_2)$  using Eq. (4) as in Sec. IV A 1. Using ion cyclotron resonance, McMahon and co-workers<sup>2</sup> bracket the fluoride affinity of carbon dioxide as  $D_0(\text{F}^–\text{CO}_2) = 31.7 \pm 2$  kcal/mol. Hiraoka *et al.*<sup>4</sup> find a slightly higher value of 32.3 kcal/mol but report no estimated uncertainty for their value. Substitution of McMahon's dissociation energy into Eq. (4) yields  $D_0(\text{F}–\text{CO}_2) = 11.5 \pm 3$  kcal/mol (0.5 eV), substantially larger than the value of  $D_0(\text{F}–\text{CO}_2) = 3.6$  kcal/mol calculated by Francisco.<sup>47</sup>  $D_0(\text{FCO}_2)$  will be larger than 11.5 kcal/mol if peak A represents photodetachment to a vibrationally excited level of the  $\text{FCO}_2 \tilde{X}^2B_2$  ground state rather than a transition to the origin of this state.

Carbon–fluorine bond strengths for other halocarbon compounds are measured to be  $\sim 100$  kcal/mol. For example,  $D_0(\text{H}_3\text{C}–\text{F}) = 109.9 \pm 1$  kcal/mol,  $D_0(\text{F}_3\text{C}–\text{F}) = 130.5 \pm 1$  kcal/mol,  $D_0(\text{Cl}_3\text{C}–\text{F}) = 101.9 \pm 1$  kcal/mol, and  $D_0(\text{F}_2\text{HC}–\text{F}) = 85.3 \pm 1$  kcal/mol.<sup>48</sup> Compared to other C–F bond strengths, both the  $\text{FCO}_2^-$  and  $\text{FCO}_2$  molecules have quite weak C–F bonds. As McMahon and Northcott<sup>2(b)</sup> point out for  $\text{FCO}_2^-$  (and for  $\text{FCO}_2$ ), the C–F bond is weak because its formation requires a perturbation of the strong  $\pi$ -bonding of the  $\text{CO}_2$  molecule.

It is also interesting to compare the C–F bond lengths and bond dissociation energies for  $\text{FCO}_2$  and  $\text{FCO}_2^-$ . Although the C–F bond enthalpy of  $\text{FCO}_2^-$  is measured to be approximately triple that of  $\text{FCO}_2$ , the C–F bond length is predicted to be  $\sim 0.2$  Å longer in the anion. All of the neutral  $\text{FCO}_2$  electronic states studied are predicted to have C–F bond lengths on the order of 1.35 Å, even though the un-

paired electron occupies a different orbitals for each state. Thus, it is likely that the C–F bond extension in  $\text{FCO}_2^-$  results from the diffuse nature of the additional charge rather than from the bonding character of the orbital in which the extra electron resides.

The  $\text{FCO}_2$  heat of formation,  $\Delta_f H_{298}^0(\text{FCO}_2)$  can be obtained using Eq. (13) from the measured  $\text{EA}(\text{FCO}_2) = 4.277 \pm 0.030$  eV, the  $\text{FCO}_2^-$  heat of formation,  $\Delta_f H_{298}^0(\text{FCO}_2^-) = -185 \pm 2.6$  kcal/mol (8.02 eV  $\pm 0.11$  eV),<sup>2(a)</sup> and a combination of measured and calculated vibrational frequencies,

$$\Delta_f H_{298}^0(\text{FCO}_2) = \Delta_f H_{298}^0(\text{FCO}_2^-) + \text{EA}(\text{FCO}_2) + \frac{5}{2} RT + \int_0^{298 \text{ K}} [C_p(\text{FCO}_2) - C_p(\text{FCO}_2^-)] dT. \quad (13)$$

Here the  $5/2RT$  term (1.481 kcal/mol; 0.064 eV) accounts for the heat capacity of the electron.<sup>49</sup> The three symmetric stretch vibrational frequencies used in the FC simulations (Table VIII) are combined with the MP4/6-31+G vibrational frequencies for the other three modes of the neutral and the QCISD/6-31G\* frequencies of the anion to calculate the heat capacities of  $\text{FCO}_2$  and  $\text{FCO}_2^-$ . Substitution into Eq. (13) yields  $\Delta_f H_{298}^0(\text{FCO}_2) = -85.2 \pm 2.8$  kcal/mol ( $-3.69 \pm 0.12$  eV).

In light of the weak C–F bond found in the  $\text{FCO}_2$  radical, the amount of vibrational structure observed in the  $\text{FCO}_2^-$  photoelectron spectrum is quite surprising. Both the  ${}^2B_2$  and  ${}^2A_2$  electronic states of  $\text{FCO}_2$  correlate adiabatically to the  $\text{F}({}^2P) + \text{CO}_2({}^1\Sigma_g^+)$  dissociation products.<sup>10</sup> All peaks at eKE's less than

$$\text{eKE} = h\nu - D_0(\text{FCO}_2^-) - \text{EA}(\text{F}) \quad (14)$$

correspond to energy levels of the neutral with enough energy to dissociate to  $\text{F} + \text{CO}_2$ ; this value is indicated by the arrow in Fig. 4. This shows that all of the peaks associated with the  ${}^2A_2$  state represent transitions to levels of  $\text{FCO}_2$  which are energetically unstable with respect to dissociation into  $\text{F} + \text{CO}_2$  products. The peaks, known to be broadened due to space-charge effects and combination band congestion, remain reasonably well resolved at energies more than 0.5 eV above this dissociation asymptote. The retention of reasonably narrow peak widths indicates that molecules excited to these vibrational levels must survive for at least a vibrational period, and perhaps longer, before dissociation.

This behavior, which was also seen for the excited states of  $\text{O}_3$  in the  $\text{O}_3^-$  photoelectron spectrum,<sup>50</sup> suggests that either a potential energy barrier prevents prompt dissociation, or that the potential energy surface for the  ${}^2A_2$  state is rather flat along the dissociation coordinate in the Franck–Condon region for photodetachment. Francisco *et al.*<sup>12</sup> did not find a barrier saddle point along the  $\text{FCO}_2 \tilde{X}^2B_2 \rightarrow \text{F}({}^2P) + \text{CO}_2({}^1\Sigma_g^+)$  dissociation coordinate at the MP2/3-21G level of theory. A similar search was also made along the dissociation coordinate of the lower symmetry  ${}^2A'$  structure predicted by MP2 theory, which correlates to the  ${}^2A_2$  state in  $C_{2v}$  symmetry. Here they found a barrier of 0.72 eV with respect to the



bound species (0.66 eV with respect to the separated products). The existence of such a barrier for the  ${}^2A_2$  state is sufficient to explain the observed vibrational structure for that state. However, it would be useful to explore the barrier height in a higher level calculation for which symmetry breaking of  ${}^2A_2$  state does not occur.

## V. CONCLUSIONS

Negative ion photoelectron spectroscopy has been used to investigate the  $X^-(CO_2)$  clusters ( $X=I, Br, Cl$ , and  $F$ ). The spectra indicate that the bonding in  $I^-(CO_2)$ ,  $Br^-(CO_2)$ , and  $Cl^-(CO_2)$  clusters is primarily electrostatic, being dominated by a charge-quadrupole interaction. This interaction leads to a distortion of the  $CO_2$  molecule producing Y-shaped anions. Franck-Condon analyses of the data show that the OCO angle in the  $I^-(CO_2)$ ,  $Br^-(CO_2)$ , and  $Cl^-(CO_2)$  clusters is  $174.5 \pm 1.5^\circ$ ,  $172.2 \pm 1.5^\circ$ , and  $169.2 \pm 2.5^\circ$ , respectively. Reasonable agreement is found between experimental and *ab initio* results for the  $Cl^-(CO_2)$  cluster. Electrostatic calculations excluding charge transfer were shown to predict OCO bond angles in the  $X^-(CO_2)$  anions which were very close to the experimental values, indicating that the primary mechanism for distortion of the  $CO_2$  from linearity is the  $X^-/CO_2$  electrostatic interaction.

The  $FCO_2^-$  photoelectron spectrum shows that both the  $FCO_2^-$  and  $FCO_2$  molecules have more covalent bonding character than the other systems studied. However, these bonds are also found to be fairly weak [ $D_0(F^-CO_2)=31.7 \pm 2$  kcal/mol (Refs. 2 and 4) and  $D_0(F-CO_2)=11.5$  kcal/mol] when compared to other known C-F chemical bonds ( $\sim 100$  kcal/mol). The weakness of the C-F bond is attributed to the stability of the C-O bonds which must be lost in the formation of the C-F bond. The  $FCO_2$  heat of formation is determined to be  $\Delta_f H_{298}^0(FCO_2) = -85.2 \pm 2.8$  kcal/mol. Two electronic states of  $FCO_2$  are observed. These are assigned as the  $\tilde{X}^2B_2$  ground state and the previously unobserved  $\tilde{A}^2A_2$  first excited state. The spectra exhibit vibrational progressions which extend well above the dissociation asymptote for both of these states indicating that a substantial barrier to dissociation exists for the  ${}^2A_2$  state. Franck-Condon simulations of the data using *ab initio* geometries and force constants calculated for the  $FCO_2^-$  anion and the  $FCO_2$   ${}^2B_2$  and  ${}^2A_2$  electronic states reproduce the major features of the experimental data remarkably well.

*Note added in proof.* Our heat of formation for  $FCO_2$  agrees well with a new value,  $-86.0$  kcal/mol, calculated by Francisco.<sup>44</sup>

## ACKNOWLEDGMENTS

This work has been supported by the United States Air Force Office of Scientific Research under Contract No. F49620-94-1-0115. We thank Professor Martin Head-Gordon for helpful suggestions with the *ab initio* calculations.

<sup>1</sup>(a) K. G. Spears, J. Chem. Phys. **57**, 1850 (1972); (b) K. G. Spears and E. Ferguson, *ibid.* **59**, 4174 (1973).

<sup>2</sup>(a) J. W. Larson and T. B. McMahon, J. Am. Chem. Soc. **107**, 766 (1985);

(b) T. B. McMahon and C. J. Northcott, Can. J. Chem. **56**, 1069 (1978).  
<sup>3</sup>R. G. Keese, N. Lee, and A. W. Castleman, Jr., J. Chem. Phys. **73**, 2195 (1980).  
<sup>4</sup>K. Hiraoka, S. Mizuse, and S. Yamabe, J. Chem. Phys. **87**, 3647 (1987); K. Hiraoka, T. Shoda, K. Morise, S. Yamabe, E. Kawai, and K. Hiraoka, *ibid.* **84**, 2091 (1986).  
<sup>5</sup>B. S. Ault, Inorg. Chem. **21**, 756 (1982).  
<sup>6</sup>G. Markovich, R. Giniger, M. Levin, and O. Cheshnovsky, Z. Phys. D **20**, 69 (1991).  
<sup>7</sup>D. W. Arnold, S. E. Bradforth, E. H. Kim, and D. M. Neumark, J. Chem. Phys. **97**, 9468 (1992).  
<sup>8</sup>Y. Zhao, C. C. Arnold, and D. M. Neumark, J. Chem. Soc. Faraday Trans. 2 **89**, 1449 (1993).  
<sup>9</sup>M. T. Nguyen, J. Mol. Struct. **133**, 269 (1985).  
<sup>10</sup>J. S. Francisco and A. Ostafin, J. Phys. Chem. **94**, 6337 (1990).  
<sup>11</sup>G. Hancock and D. E. Heard, J. Chem. Soc. Faraday Trans. 2 **87**, 1039 (1991); **87**, 1045 (1991).  
<sup>12</sup>J. S. Francisco, A. N. Goldstein, Z. Li, Y. Zhao, and I. H. Williams, J. Phys. Chem. **94**, 4791 (1990); J. S. Francisco, Chem. Phys. Lett. **163**, 375 (1989); J. S. Francisco and A. N. Goldstein, Chem. Phys. **127**, 73 (1988).  
<sup>13</sup>M. M. Maricq, J. J. Szente, Z. Li, and J. S. Francisco, J. Chem. Phys. **98**, 784 (1993).  
<sup>14</sup>M. M. Maricq, J. J. Szente, G. A. Khitrov, and J. S. Francisco, J. Chem. Phys. **98**, 9522 (1993).  
<sup>15</sup>T. J. Wallington, T. Ellermann, O. J. Nielsen, and J. Sehested, J. Phys. Chem. **98**, 2346 (1994).  
<sup>16</sup>D. M. Cyr, M. G. Scartron, and M. A. Johnson, J. Chem. Phys. **99**, 4869 (1993).  
<sup>17</sup>R. B. Metz, A. Weaver, S. E. Bradforth, T. N. Kitsopoulos, and D. M. Neumark, J. Phys. Chem. **94**, 1377 (1990).  
<sup>18</sup>M. A. Johnson, M. L. Alexander, and W. C. Lineberger, Chem. Phys. Lett. **112**, 285 (1984).  
<sup>19</sup>W. C. Wiley and I. H. McLaren, Rev. Sci. Instrum. **26**, 1150 (1955).  
<sup>20</sup>J. Cooper and R. N. Zare, J. Chem. Phys. **48**, 942 (1968).  
<sup>21</sup>J. Simons, J. Phys. Chem. **95**, 1017 (1991); J. Simons and K. D. Jordan, Chem. Rev. **87**, 535 (1987).  
<sup>22</sup>GAUSSIAN 92, Revision C, M. J. Frisch, G. W. Trucks, M. Head-Gordon, P. M. W. Gill, M. W. Wong, J. B. Foresman, B. G. Johnson, H. B. Schlegel, M. A. Robb, E. S. Replogle, R. Gomperts, J. L. Andres, K. Raghavachari, J. S. Binkley, C. Gonzalez, R. L. Martin, D. J. Fox, D. J. Defrees, J. Baker, J. J. P. Stewart, and J. A. Pople, Gaussian, Inc., Pittsburgh, Pennsylvania, 1992.  
<sup>23</sup>The C-O bond length is the same bond length used in electrostatic calculations described in Sec. IV A 2. The value results from an optimization of the  $CO_2$  geometry at the HF/6-31+G\* level of theory.  
<sup>24</sup>Quadratic Configuration Interaction with Single and Double excitations.  
<sup>25</sup>D. Ovenall and D. H. Whiffen, Mol. Phys. **4**, 135 (1961); J. E. Bennett, B. Mile, and A. Thomas, Trans. Faraday Soc. **61**, 2357 (1965).  
<sup>26</sup>Note that a force constant analysis indicates that the geometry calculated for the  ${}^2B_1$  state is not at a potential energy minimum but at a saddle point.  
<sup>27</sup>The calculated geometry for the  $C_s$  species at MP2/6-31+G\*;  $R_{CF}=1.339$  Å;  $R_{CO}=1.170$  Å;  $R_{CO'}=1.392$  Å;  $\angle OCO'=126.6^\circ$ ;  $\angle FCO=124.7^\circ$ .  
<sup>28</sup>A. D. McLean, B. H. Lengsfeld III, J. Pacansky, and Y. Ellinger, J. Chem. Phys. **83**, 3567 (1985).  
<sup>29</sup>N. A. Burton, Y. Yamaguchi, I. L. Alberts, and H. F. Schaefer III, J. Chem. Phys. **95**, 7466 (1991); C. P. Blahous III, B. F. Yates, Y. Xie, and H. F. Schaefer III, *ibid.* **93**, 8105 (1990).  
<sup>30</sup>A. J. Stone, Chem. Phys. Lett. **83**, 233 (1981); S. L. Price, A. J. Stone, and M. Alderton, Mol. Phys. **32**, 987 (1984); A. J. Stone and M. Alderton, *ibid.* **56**, 1047 (1985).  
<sup>31</sup>M. R. Battaglia, A. D. Buckingham, D. Neumark, R. K. Pierens, and J. H. Williams, Mol. Phys. **43**, 1015 (1981).  
<sup>32</sup>C. S. Yeh, K. F. Willey, D. F. Robbins, J. S. Pilgrim, and M. A. Duncan, J. Chem. Phys. **98**, 1867 (1993); C. S. Yeh, K. F. Willey, D. L. Robbins, and M. A. Duncan, *ibid.* **96**, 7833 (1992).  
<sup>33</sup>M. A. Pariseau, I. Suzuki, and J. Overend, J. Chem. Phys. **42**, 2335 (1965).  
<sup>34</sup>G. Herzberg, *Molecular Spectra and Molecular Structure III. Electronic Spectra and Electronic Structure of Polyatomic Molecules* (Krieger, Malabar, 1991).  
<sup>35</sup>H. S. W. Massey, *Negative Ions* (Cambridge University, Cambridge, 1976); K. Ervin, J. Ho, and W. C. Lineberger, J. Chem. Phys. **91**, 5974 (1991).

- <sup>36</sup>V. Aquilanti, D. Cappelletti, and F. Pirani, *J. Chem. Soc. Faraday Trans.* **89**, 1467 (1993).
- <sup>37</sup>R. N. Dixon, *Proc. R. Soc.* **275A**, 431 (1963).
- <sup>38</sup>R. D. Amos and J. E. Rice, CADPAC, The Cambridge Analytical Derivatives Package, issue 4.0, Cambridge, 1987.
- <sup>39</sup>I. Suzuki, *J. Mol. Spectrosc.* **25**, 479 (1968).
- <sup>40</sup>A. D. Buckingham, *Quart. Rev. Chem. Soc. London* **13**, 183 (1959).
- <sup>41</sup>A. A. S. Sangachin and J. Shanker, *J. Chem. Phys.* **90**, 1061 (1989).
- <sup>42</sup>A. D. Buckingham and P. W. Fowler, *Can. J. Chem.* **63**, 2018 (1985); A. D. Buckingham, P. W. Fowler, and A. J. Stone, *Int. Rev. Phys. Chem.* **5**, 107 (1986).
- <sup>43</sup>The  $R_{X-C}=3.77$  Å distance assumes  $\theta=174.5^\circ$ .
- <sup>44</sup>T. S. Dibble and J. S. Francisco, *J. Phys. Chem.* **98**, 11694 (1994).
- <sup>45</sup>A. Weaver, D. W. Arnold, S. E. Bradforth, and D. M. Neumark, *J. Chem. Phys.* **94**, 1740 (1991).
- <sup>46</sup>E. B. Wilson, Jr., J. C. Decius, and P. C. Cross, *Molecular Vibrations* (Dover, New York, 1980).
- <sup>47</sup>Although the antisymmetric stretch force constants (fc's) suffer from numerical errors, the normal coordinates appear to be less affected and are used for comparison to the  $^2A_2$  results. Simulations using HF and MP2 fc's produce very similar results.
- <sup>48</sup>From Ref. 10, using their PMP4SDTQ/6-31G\*\*/UMP2/6-31G\* +  $\Delta ZPE$ /UMP2/6-31+G\* values.
- <sup>49</sup>D. F. McMillen and D. M. Golden, *Annu. Rev. Phys. Chem.* **33**, 493 (1982).
- <sup>50</sup>S. G. Lias, J. E. Bartmess, J. F. Liebman, J. L. Holmes, R. D. Levin, and W. G. Mallard, *J. Phys. Chem. Ref. Data* **17**, Suppl. 1, 5 (1988).
- <sup>51</sup>D. W. Arnold, C. Xu, E. H. Kim, and D. M. Neumark, *J. Chem. Phys.* **101**, 912 (1994).